Carbon Dioxide Capture for Storage in Deep Geologic Formations – Results from the CO_2 Capture Project

Geologic Storage of Carbon Dioxide with Monitoring and Verification

Volume 2

Elsevier Internet Homepage – http://www.elsevier.com
Consult the Elsevier homepage for full catalogue information on all books, major reference works, journals, electronic products and services.

Elsevier Titles of Related Interest

AN END TO GLOBAL WARMING
L.O. Williams
ISBN: 0-08-044045-2, 2002

FUNDAMENTALS AND TECHNOLOGY OF COMBUSTION
F. El-Mahallawy, S. El-Din Habik
ISBN: 0-08-044106-8, 2002

GREENHOUSE GAS CONTROL TECHNOLOGIES: 6TH INTERNATIONAL CONFERENCE
John Gale, Yoichi Kaya
ISBN: 0-08-044276-5, 2003

MITIGATING CLIMATE CHANGE: FLEXIBILITY MECHANISMS
T. Jackson
ISBN: 0-08-044092-4, 2001

Related Journals:
Elsevier publishes a wide-ranging portfolio of high quality research journals, encompassing the energy policy, environmental, and renewable energy fields. A sample journal issue is available online by visiting the Elsevier web site (details at the top of this page). Leading titles include:

Energy Policy
Renewable Energy
Energy Conversion and Management
Biomass & Bioenergy
Environmental Science & Policy
Global and Planetary Change
Atmospheric Environment
Chemosphere – Global Change Science
Fuel, Combustion & Flame
Fuel Processing Technology

All journals are available online via ScienceDirect: www.sciencedirect.com

To Contact the Publisher
Elsevier welcomes enquiries concerning publishing proposals: books, journal special issues, conference proceedings, etc. All formats and media can be considered. Should you have a publishing proposal you wish to discuss, please contact, without obligation, the publisher responsible for Elsevier's Energy program:

Henri van Dorssen
Publisher
Elsevier Ltd
The Boulevard, Langford Lane
Kidlington, Oxford
OX5 1GB, UK

Phone: +44 1865 84 3682
Fax: +44 1865 84 3931
E.mail: h.dorssen@elsevier.com

General enquiries, including placing orders, should be directed to Elsevier's Regional Sales Offices – please access the Elsevier homepage for full contact details (homepage details at the top of this page).

Carbon Dioxide Capture for Storage in Deep Geologic Formations – Results from the CO_2 Capture Project

Geologic Storage of Carbon Dioxide with Monitoring and Verification

Edited by

Sally M. Benson
Lawrence Berkeley Laboratory
Berkeley, CA,USA

and Associate Editors

Curt Oldenburg[1], Mike Hoversten[1] and Scott Imbus[2]
[1]Lawrence Berkeley National Laboratory
Berkeley, CA, USA
[2]Chevron Texaco Energy Technology Company
Bellaive, TX, USA

Volume 2

ELSEVIER
2005

Amsterdam – Boston – Heidelberg – London – New York – Oxford
Paris – San Diego – San Francisco – Singapore – Sydney – Tokyo

ELSEVIER B.V.
Radarweg 29
P.O. Box 211, 1000 AE Amsterdam
The Netherlands

ELSEVIER Inc.
525 B Street, Suite 1900
San Diego, CA 92101-4495
USA

ELSEVIER Ltd
The Boulevard, Langford Lane
Kidlington, Oxford OX5 1GB
UK

ELSEVIER Ltd
84 Theobalds Road
London WC1X 8RR
UK

First edition 2005

Library of Congress Cataloging in Publication Data
A catalog record is available from the Library of Congress.

British Library Cataloguing in Publication Data
A catalogue record is available from the British Library.

ISBN: 0-08-044570-5 (2 volume set)

Volume 1: Chapters 8, 9, 13, 14, 16, 17, 18, 24 and 32 were written with support of the U.S. Department of Energy under Contract No. DE-FC26-01NT41145. The Government reserves for itself and others acting on its behalf a royalty-free, non-exclusive, irrevocable, worldwide license for Governmental purposes to publish, distribute, translate, duplicate, exhibit and perform these copyrighted papers. EU co-funded work appears in chapters 19, 20, 21, 22, 23, 33, 34, 35, 36 and 37. Norwegian Research Council (Klimatek) co-funded work appears in chapters 1, 5, 7, 10, 12, 15 and 32.

Volume 2: The Storage Preface, Storage Integrity Preface, Monitoring and Verification Preface, Risk Assessment Preface and Chapters 1, 4, 6, 8, 13, 17, 18, 19, 20, 21, 22, 23, 24, 25, 26, 27, 28, 29, 30, 31, 32, 33 were written with support of the U.S. Department of Energy under Contract No. DE-FC26-01NT41145. The Government reserves for itself and others acting on its behalf a royalty-free, non-exclusive, irrevocable, worldwide license for Governmental purposes to publish, distribute, translate, duplicate, exhibit and perform these copyrighted papers. Norwegian Research Council (Klimatek) co-funded work appears in chapters 9, 15 and 16.

♾ The paper used in this publication meets the requirements of ANSI/NISO Z39.48-1992 (Permanence of Paper).
Printed in The Netherlands.

Carbon Dioxide Capture for Storage in Deep Geologic Formations, Volume 2
D.C. Thomas and S.M. Benson (Eds.)

Chapter 23

NON-SEISMIC GEOPHYSICAL APPROACHES TO MONITORING

G.M. Hoversten and Erika Gasperikova

Lawrence Berkeley National Laboratory, Berkeley, CA, U.S.A.

ABSTRACT

This chapter considers the application of a number of different geophysical techniques for monitoring geologic storage of CO_2. The relative merits of the seismic, gravity, electromagnetic (EM) and streaming potential (SP) geophysical techniques as monitoring tools are examined. An example of tilt measurements illustrates another potential monitoring technique, although it has not been studied to the extent of other techniques in this chapter. This work does not represent an exhaustive study, but rather demonstrates the capabilities of a number of geophysical techniques on two synthetic modeling scenarios. The first scenario represents combined CO_2 enhance oil recovery (EOR) and storage in a producing oil field, the Schrader Bluff field on the north slope of Alaska, USA. The second scenario is of a pilot DOE CO_2 storage experiment scheduled for summer 2004 in the Frio Brine Formation in South Texas, USA. Numerical flow simulations of the CO_2 injection process for each case were converted to geophysical models using petrophysical models developed from well log data. These coupled flow simulation–geophysical models allow comparison of the performance of monitoring techniques over time on realistic 3D models by generating simulated responses at different times during the CO_2 injection process. These time-lapse measurements are used to produce time-lapse changes in geophysical measurements that can be related to the movement of CO_2 within the injection interval.

The time-lapse performance of seismic, gravity, and EM techniques are considered for the Schrader Bluff model. Surface gravity, surface tilt and SP measurements are considered for the Frio brine formation model. These two models represent end members of a complex spectrum of possible storage scenarios. EOR/storage projects in general and Schrader Bluff in particular represent relatively thin injection intervals with multiple fluid components (oil, hydrocarbon gas, brine, and CO_2) while brine formations such as the Frio will usually have much thicker injection intervals and only two component (brine and CO_2) systems.

INTRODUCTION

Cost effective monitoring of reservoir fluid movement during CO_2 storage is a necessary part of a practical geologic storage strategy.

In this chapter, we evaluate seismic and alternative approaches for long-term monitoring. In order to evaluate alternative geophysical monitoring techniques two numerical simulations of CO_2 storage scenarios are considered. The time-lapse performance of seismic, gravity, and EM techniques are examined using models derived from reservoir flow simulation of the CO_2 EOR/storage process for the Schrader Bluff reservoir on the North Slope of Alaska, USA. Surface gravity, surface tilt, and SP measurements are considered for the Frio brine formation test in south Texas, USA. These two models represent end members of a complex spectrum of possible storage scenarios. EOR/storage projects in general and Schrader Bluff in particular represent relatively thin injection intervals with multiple fluid components (oil, hydrocarbon gas, brine, and CO_2) while brine formations will usually have much thicker potential injection intervals and only two component (brine and CO_2) systems.

Petroleum reservoirs and brine formations offer the two most obvious storage targets. Petroleum reservoirs have the natural advantages that they are already well characterized, have a demonstrated seal, have

an existing infrastructure, and offer cost offsets in the form of enhanced petroleum production as CO_2 is injected. From a monitoring standpoint, petroleum reservoirs offer more challenges than brine formations because they typically have less vertical extent (~25 m for oil vs. hundreds of meter for brine formations) and have multiple in situ fluids. Not withstanding their inherent monitoring challenges, petroleum reservoir will undoubtedly provide many of the early storage examples.

We have chosen to include seismic modeling of the Schrader Bluff scenario for comparison with the non-seismic techniques. While the work presented here is all forward modeling of responses, future work will concentrate on inversion of data to produce quantitative estimates of reservoir properties from the various techniques. Simulation of the seismic response for the same models considered for non-seismic techniques will allow a side-by-side quantitative comparison. Within the seismic modeling section for Schrader Bluff we have included some models appropriate for brine formations using a published rock-properties model.

The Schrader Bluff model used here for analysis began with a three dimensional (3D) flow simulation model provided by BP Alaska. In addition, we developed a detailed rock-properties model from log data that provides the link between the reservoir parameters (porosity, pressure, saturations, etc.) and the geophysical parameters (velocity, density, electrical resistivity). The rock-properties model was used to produce geophysical models from the flow simulations. The same procedures were used to produce numerical models for the Frio brine formation pilot test.

On-shore EOR project—Schrader Bluff, Alaska

One site being considered for geologic storage is the Schrader Bluff reservoir on Alaska's North Slope (Figure 1). Preliminary evaluations show that a CO_2-based enhanced oil recovery could increase oil recovery by up to 50% over water-flooding [1]. Furthermore, the studies concluded that up to 60% of the CO_2 injected as part of the EOR scheme would remain in the reservoir. A schematic geological cross-section through the Schrader Bluff Formation is shown in Figure 2.

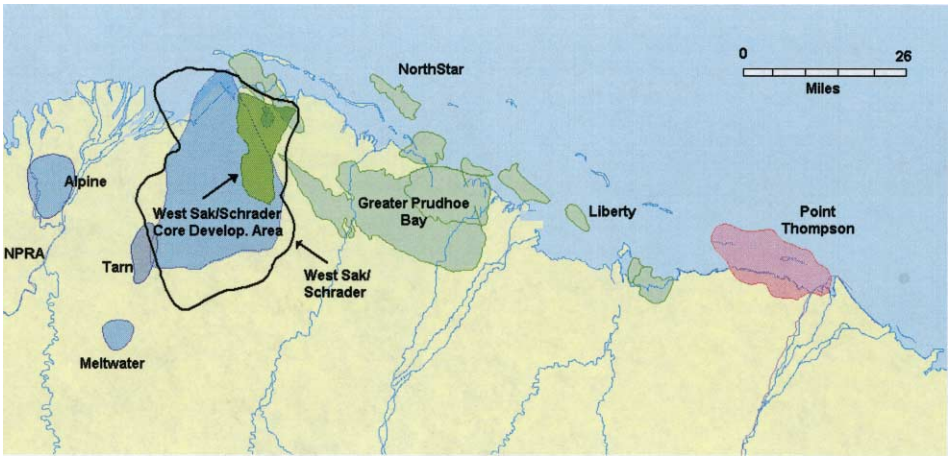

Figure 1: Location of Schrader Bluff reservoir on Alaska's North Slope.

In order to compare the spatial resolution and sensitivity of various geophysical techniques being considered for CO_2 storage monitoring, a 3D flow simulation model of the reservoir provided by BP was used in conjunction with rock-properties relations developed from log data to produce geophysical models from the flow simulations. The Schrader Bluff reservoir is a sandstone unit, between 25 and 30 m

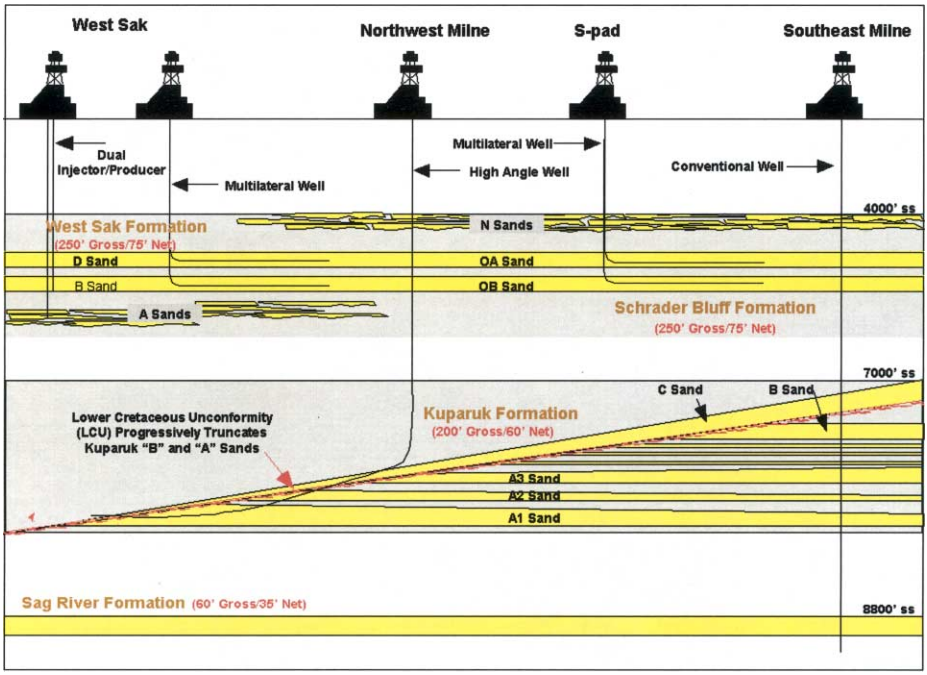

Figure 2: A schematic geological cross-section through the Schrader Bluff Formation.

thick, at a depth of 1100–1400 m. Figure 3 shows a 3D view of the portion of the reservoir under consideration for a CO_2 storage test. The reservoir unit gently dips to the east with major faulting running mainly north–south. Two faults with offsets in excess of 75 m cut the reservoir with several smaller sub-parallel faults present. Time-lapse snap shots of the reservoir at initial conditions and 5-year increments out to 2035 were used. A water after gas (WAG) injection strategy is considered which produces complicated spatial variations in fluid (CO_2, brine, oil and gas) saturation within the reservoir over time.

Rock-properties model

A rock-properties model was developed from log data for the reservoir. This model relates reservoir parameters to geophysical parameters, and is used to convert the flow simulation model parameters to geophysical parameters (acoustic velocity V_p, shear velocity V_s, density and electrical resistivity). We have assumed the unconsolidated sand model where the effective pressure is equal to lithostatic pressure minus the pore pressure. As noted by Brandt [2] as cementation of the sand grains increases the effective pressure would be the lithostatic minus some fraction of the pore pressure. Pressure effects are included through the effective pressure on the dry frame and through the effects of pore pressure on the fluids used in the Gassmann fluid substitutions. A description of the rock-properties modeling process is given by Hoversten et al. [3]. Archie's law is used for electrical resistivity as a function of porosity and water saturation. Figure 4 shows the rock-properties parameters along with the predicted values of V_p, V_s and density compared to the log values from the MPS-15 well. The model V_p, derived from the flow simulation, at initial conditions is shown in Figure 4 on a east–west cross-section through two injection wells.

A critical porosity [4] appropriate for sandstone of 35% was assumed. Oil API gravity and brine salinity are taken from measured values. The regression-determined values of the grain shear modulus and Poisson ratio are appropriate for quartz grains. The model parameters are determined for the reservoir interval in the logs. The full geophysical models are built by interpolating available well logs in 3D using the seismic reservoir

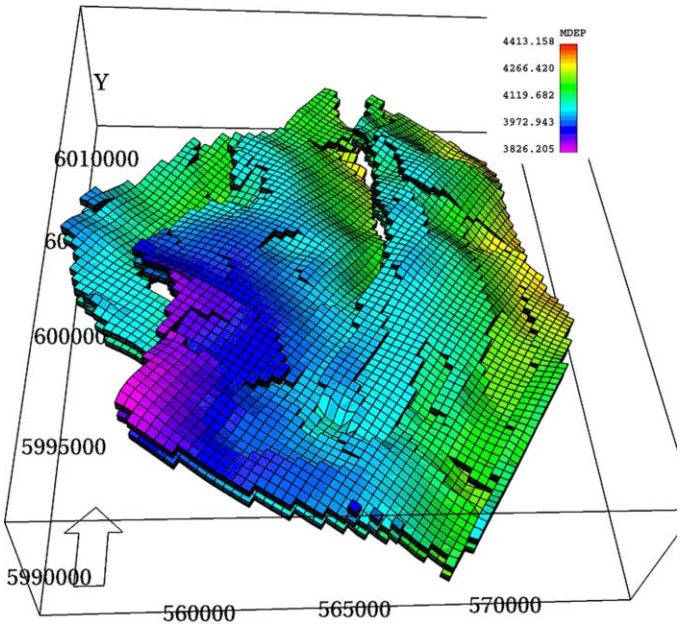

Figure 3: Three-dimensional view of the portion of the reservoir under consideration for CO_2 sequestration test at Schrader Bluff. Depths range between 3800 and 4400 ft (1158 and 1341 m) true vertical depth.

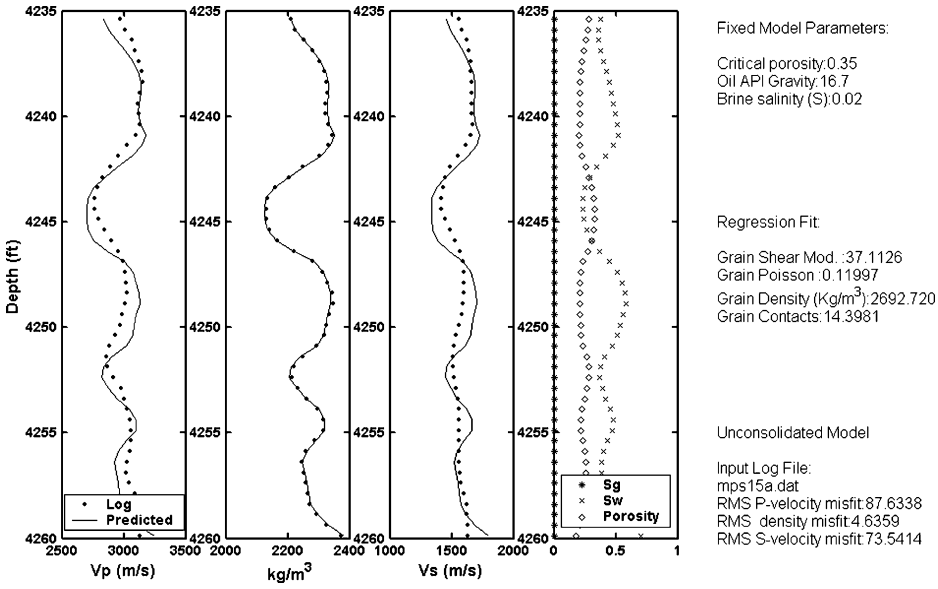

Figure 4: Rock-properties model based on un-consolidated sandstone model [4]. Measured log values shown as dots. Parameters (right side) are derived from a simplex minimization of the misfit between observed and calculated V_p, V_s and density logs. Predicted V_p, V_s and density are shown as solid lines.

surfaces as a spatial guide. This produces a background model of V_p, V_s, density, and resistivity. The reservoir flow simulations, which only cover the reservoir interval, are then filled in at the time intervals where flow simulations were done. The model shown in Figure 4, along with Archie's law, is used to convert the porosity, water saturation, oil saturation, gas saturation, CO_2 saturation, pressure, and temperature from the flow simulation to V_p, V_s, density, and electrical resistivity.

Gravity modeling

A snapshot of the model at initial conditions, before CO_2 injection begins, is shown in Figure 5. Figure 5a is an east–west cross-section of bulk density as a function of depth and horizontal distance between a pair of injection wells. In this figure, gravimeters are located in two wells roughly 8 km apart. The reservoir interval is outlined in white; the positions of the gravimeters are indicated by black squares. Since they are very closely spaced they overlap and show as an image of a well. Figure 5b is a plan view of the density at initial conditions at a depth of 1200 m with positions of 23 injecting wells taken from the reservoir simulation. The circled well location in the upper part of Figure 5b indicates a well for which borehole gravity responses are shown in Figures 11 and 12.

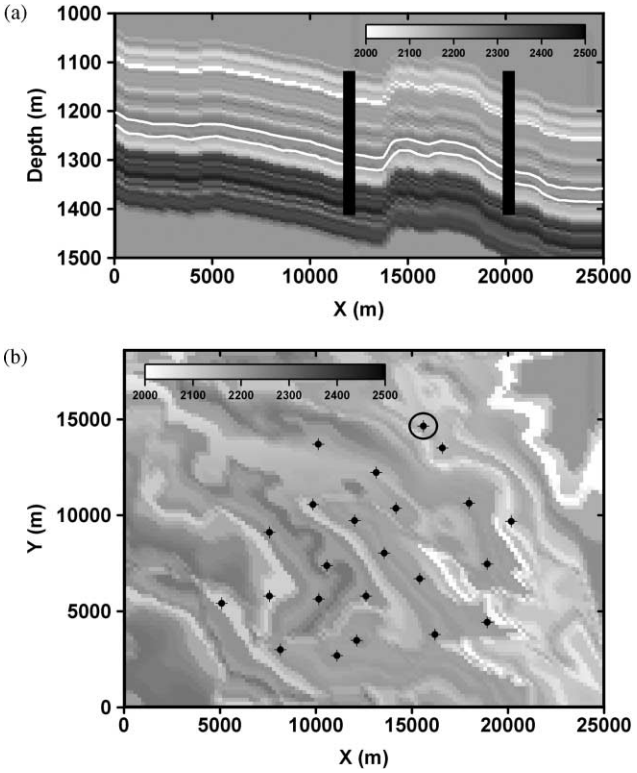

Figure 5: (a) Cross-section of a density field (kg/m^3) as a function of depth and horizontal position. (b) Plan view of a density (kg/m^3) field at a depth $z = 1200$ m. The circled well indicates the well location used for borehole gravity calculations shown in Figures 11 and 12.

The surface gravity response was calculated on a grid of stations with 1 km spacing from 2000 to 22,000 m in the x direction, and from 2000 to 16,000 m in the y direction. In general, since CO_2 is less dense (at reservoir conditions) than either oil or water, addition of CO_2 to the reservoir causes a reduction

in the measured gravitational attraction either at the surface or in a borehole. (We assumed that porosity does not vary as gas is injected.)

The change in the vertical attraction of gravity (G_z) at the ground surface between 2020 and initial conditions is overlaid as black contours in Figure 6a on the net density changes within the reservoir.

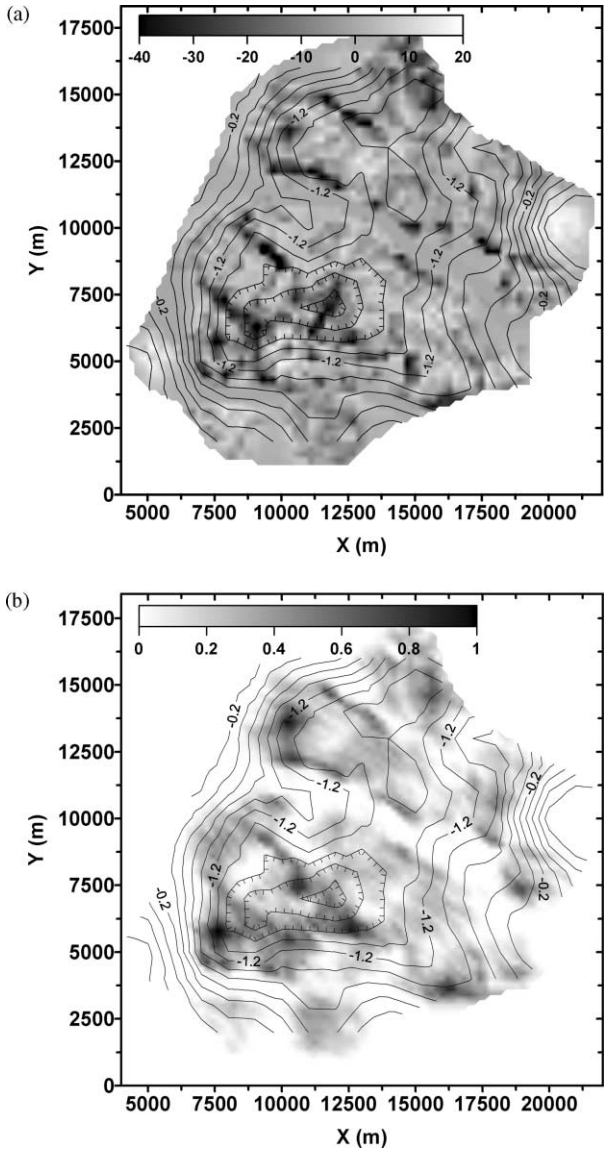

Figure 6: (a) Plan view of the net change in density (kg/m^3) within the reservoir between 2020 and initial conditions. (b) Plan view of the net changes in CO_2 saturation within the reservoir. The change in G_z at the surface for the same time interval is shown as black contours with hatch marks indicating decreasing G_z values [33].

The peak-to-peak change in G_z is on the order of 3 μgal, which is right at the level of repeatability of a field survey using current technology. The changes in the vertical gradient of gravity (dG_z/dz) between 20 years into CO_2 injection and initial conditions (not shown) are approximately 0.02 Eötvös units (EU), below the noise level of current instruments. The high spatial variations of the net density changes within the reservoir are expressed as a smoothed response at the surface (due to the depth of the reservoir) and only show the average changes on a larger scale.

It should be noted that petroleum reservoirs in general, and this reservoir in particular, are thinner (30 m) than many brine formations considered for CO_2 storage (100–200 m). This difference means that while the calculated response for Schrader Bluff at the surface are below current technology repeatability, brine formations at the same depths would produce measurable responses. This is the experience at the Sleipner CO_2 project [5] for a gravity survey conducted in 2002. These results suggest that future analysis with maximum sensitivity of G_z and dG_z/dz (that could be obtained by permanent emplacement of sensors with continuous monitoring coupled with surface deformation measurements to reduce noise levels) would be required.

Figure 6b shows the change in surface gravity G_z as black contours overlaid on the net change in CO_2 saturation within the reservoir. Because the density changes within the reservoir are caused by a combination of CO_2, water, and oil saturation changes as the WAG injection proceeds, there is not a one-to-one correlation in space between the net change in CO_2 saturation (S_{CO_2}) and the change in surface G_z. There is, however, a correlation between the change in surface G_z and the net change in S_{CO_2}, averaged on a large scale. For example, the largest changes in S_{CO_2} occur in the south–west quadrant of the image (Figure 6b) where the largest change in G_z occurs. This scenario, injecting CO_2 into an oil reservoir with multiple fluid components, is a worst case for the use of gravity to directly map changes in S_{CO_2}. In a case of CO_2 injection into a brine formation, there would only be water and CO_2, and the net changes in density within the reservoir would directly correlate with the net changes in S_{CO_2} as would the change in G_z at the surface.

Access to boreholes allows gravity measurement to be made closer to the reservoir, thus strengthening the signal compared to observations made on the surface. Figure 7a shows the change in G_z (2020–initial) at a depth of 1200 m (just above the reservoir in this section of the field), while Figure 7b is a change in dG_z/dz at the same depth. In both the figures, the data were calculated on the same grid of 1 km by 1 km site locations as on the surface. The shaded images in Figure 7a and b are the net density changes in the reservoir from Figure 6a. The changes in G_z and dG_z/dz, respectively, correlate directly with the maximum density changes. The magnitude of the changes in both G_z and dG_z/dz is larger than for surface measurements, although only the change in G_z would be measurable in the boreholes with current commercial technology. It should be noted, however, that work on more sensitive borehole G_z and dG_z/dz meters is ongoing and has the potential to significantly lower the sensitivity of such devices in the near future [6].

While Figure 7 illustrated the potential resolution by measuring close to the reservoir, access through only the existing injection wells would substantially reduce the data coverage. Figure 8a shows a map of contoured changes in G_z measured only in the 23 injection wells at a depth of 1200 m. Figure 8b is a net change of CO_2 saturation for comparison. Figure 8a was generated using a minimum curvature algorithm for data interpolation; however, it is representative of the general features present in all of the other types of interpolation tested. In general, interpretation of the interpolated G_z changes from the existing 23 boreholes would lead to an overestimate of the CO_2 saturation changes in the reservoir. This problem is particularly evident at the north end of the reservoir where increased CO_2 saturation at two isolated wells produces an interpolated image that would be interpreted as increased CO_2 between the wells where none exists. Borehole measurements need to be used in conjunction with some form of surface measurement to guide the interpolation between wells. Alternatively, pressure testing between wells could provide estimates of spatial variations in permeability that could be used to condition, in a statistical sense, interpolation of the borehole gravity data. Many possibilities exist for combining the borehole data with other information in order to produce more accurate maps of change within the reservoir. This is an area where further work could be done.

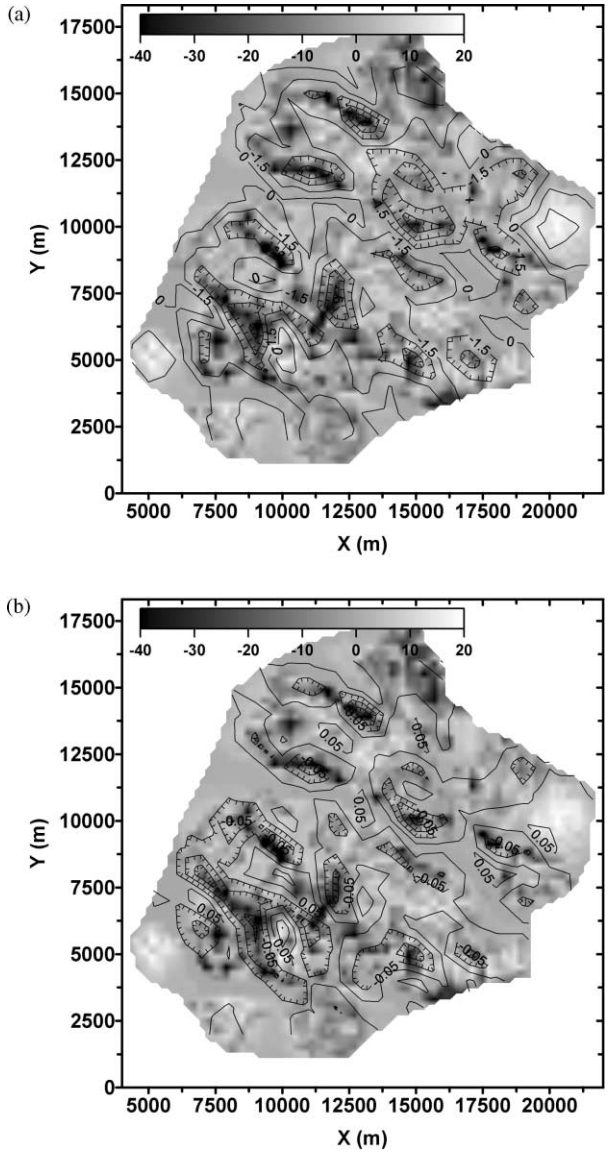

Figure 7: (a) Plan view of the net change in density (gray scale) within the reservoir (2020-initial). The change in G_z (μGal) at a depth of 1200 m is overlaid as black contours. The peak-to-peak change in G_z is approximately 10 μGal. (b) The change in dG_z/dz (EU) at a depth of 1200 m overlaid on the net change in density. The peak-to-peak change in dG_z/dz is approximately 0.3 EU.

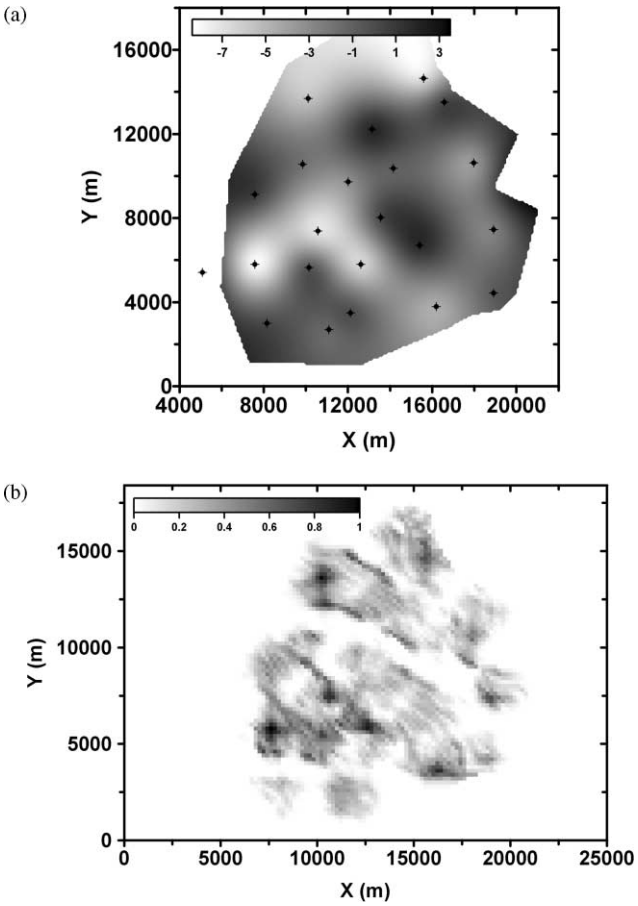

Figure 8: (a) Plan view of the change in G_z (μGal) at a depth of 1200 m between 20 years into CO_2 injection and initial conditions using 23 wells indicated by black symbols. (b) Plan view of the net change in S_{CO_2} within the reservoir between 20 years into CO_2 injection and initial condition.

In addition to considering spatial variations in G_z and dG_z/dz both on the surface and at a single depth within boreholes, the response of G_z and dG_z/dz in vertical *profiles* down boreholes was calculated. Figure 9 is the change in S_w between 2020 and initial conditions along a vertical slice through the reservoir at an injection well indicated by a circle in Figure 5b. Figure 10 shows the change in S_{CO_2} between 2020 and initial conditions. At the top of the reservoir near the injection well, S_w decreases while S_{CO_2} increases. At the bottom of the reservoir, both S_{CO_2} and S_w increase slightly. G_z measured in the borehole, shown in Figure 11a, reflects this change by a decrease in the response at the top of the reservoir, and an increase in the response at the bottom. The change in G_z is ± 8 μGal. The reservoir interval is between 1325 and 1350 m at this location. The change in G_z between 2020 and initial conditions (Figure 11b) clearly identifies the position of fluid saturation changes within the reservoir. The sign of the change reflects the changes in the local densities caused by the combined changes in all fluids (oil, brine and CO_2). The reservoir is outlined by the shaded gray area. The vertical gradient response (dG_z/dz) is shown in Figure 12a, and the change between 2020 and initial conditions is shown in Figure 12b. The change in the response is about 10 EU.

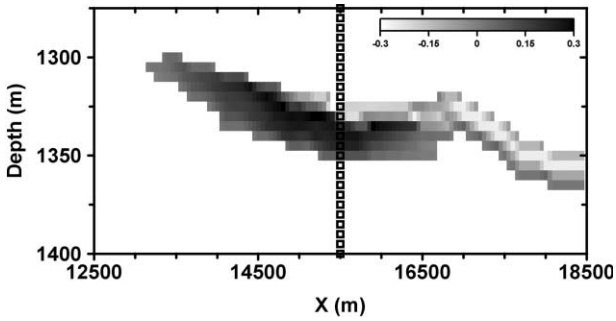

Figure 9: Change in S_w between 2020 and initial conditions. Dark colors are an increase in S_w, light colors are a decrease.

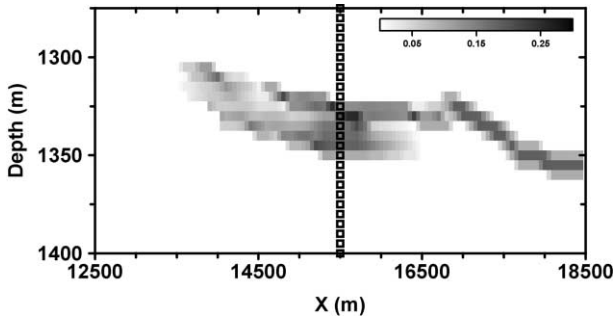

Figure 10: Change in S_{CO_2} between 2020 and initial conditions. Dark colors are an increase in S_{CO_2}, light colors are a decrease.

Popta et al. [7] showed that a geological structure with a sufficient density contrast can be detected by borehole gravity measurements if the observation well is not further away than one or two times the thickness of the zone of density contrast. Figure 13 shows a CO_2 wedge of 250 m radius and density of 2260 kg/m^3 (representing 20% CO_2 saturation in 20% porosity) inside of 100 m thick sand layer with a density of 2285 kg/m^3 at the depth of 1 km. The background density is 2160 kg/m^3. The borehole gravity response as a function of distance from the edge of the wedge is shown in Figure 14a. The maximum response at the edge of the CO_2 wedge is 10 μGal (due to 1% change in density). The responses decrease with distance away from the wedge: 50 m away from the wedge the response is 6 μGal, 100 m away response decreases to 4.4 μGal, and 200 m away it is down to 2.5 μGal. The borehole vertical gradient response for the same model is shown in Figure 14b. The response changes from 7 EU at the edge of the CO_2 wedge to 1 EU 50 m away from the edge. Current borehole gravimeter technology has a repeatability of around 5 μGal for G_z, this means that with current technology borehole measurements are sensitive to changes in a zone up to distances equal to the zone thickness away from the zone edge.

Seismic modeling

The flow simulation models for Schrader Bluff have been converted to acoustic velocity (V_p), shear velocity (V_s) and density, as previously described. A simulated seismic line (isotropic finite-difference algorithm with uniform overburden) has been calculated, running approximately N45°E across the reservoir.

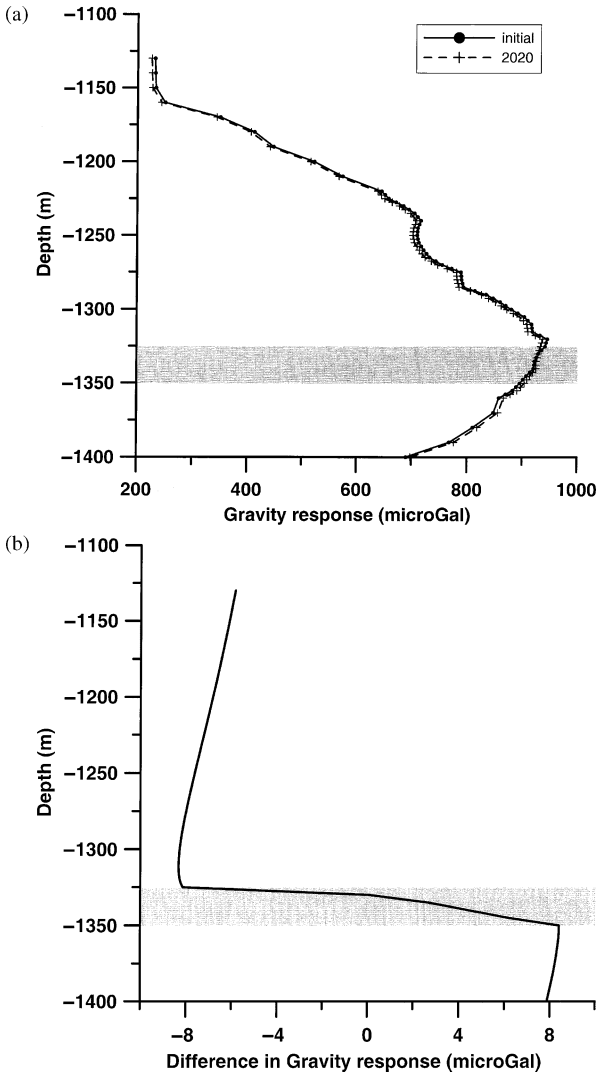

Figure 11: (a) Borehole G_z for initial conditions (circle) and 2020 (plus), (b) Change in G_z between 2020 and initial conditions. The reservoir interval is indicated by the light gray area.

The elastic response to a 50 Hz Ricker wavelet was calculated. The general increase in S_{CO_2} in portions of the reservoir near injection wells produces an approximately 20% decrease (between 2020 and 2005) in seismic velocity V_p as shown in Figure 15. The S_{CO_2} and S_w changes are shown in Figures 16 and 17, respectively. The seismic P-wave responses, for a single shot located at 7500 m (covering the area of the reservoir with maximum change in S_{CO_2}) on the 2D profile, for 2005 and 2020 are shown in Figure 18 with the difference shown in Figure 19. As discussed later, there is a significant Class 3 [8] type AVO effect as S_{CO_2} increases in the reservoir.

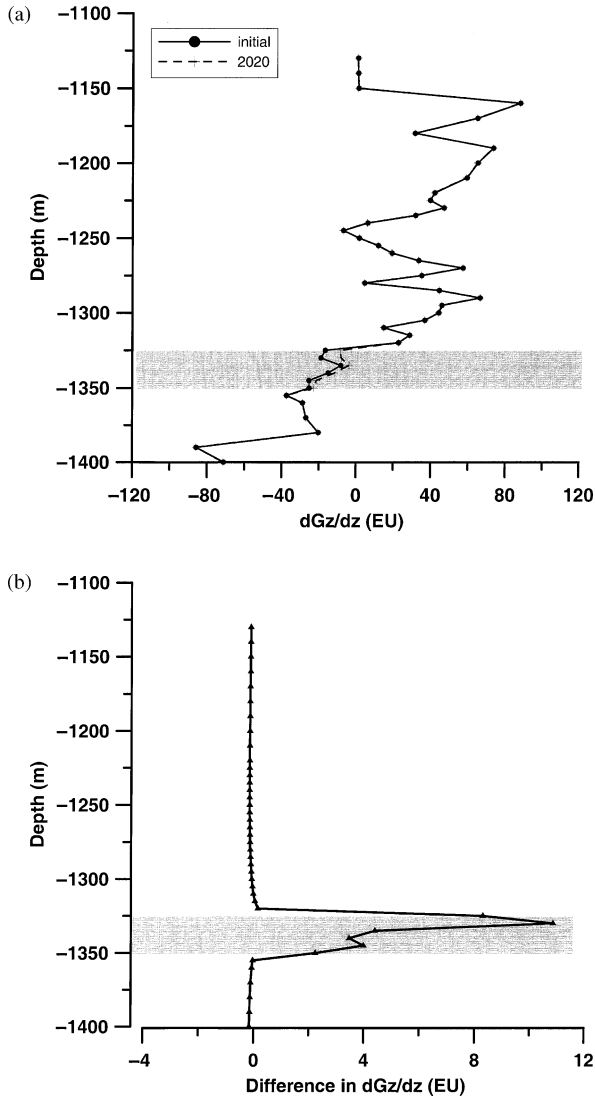

Figure 12: (a) Borehole vertical gradient response $(\mathrm{d}G_z/\mathrm{d}z)$ for initial conditions (circle) and 2020 (plus), (b) Change in $\mathrm{d}G_z/\mathrm{d}z$ between 2020 and initial conditions. The reservoir interval is indicated by the light gray area.

The P-wave response was sorted to CDP gathers, NMO corrected and stacked to produce the sections for 2005 and 2020 shown in Figure 20. The gray line is a constant time horizon within the reservoir for reference. The 30 m reservoir interval is not uniform and is comprised of 5 m thick substrata, each of which has reflection coefficients at their top and base that vary with S_{CO_2}. These sub-strata are all below the seismic tuning thickness. This produces a seismic response without a clear top and base reflector. There is a significant increase in S_{CO_2} to the right of CDP 8412.5 producing the large change in the stacked sections shown in Figure 20.

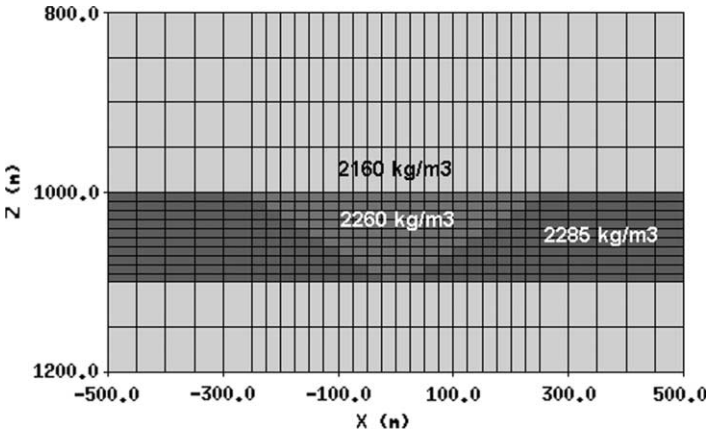

Figure 13: CO_2 wedge model.

The difference between the stacked sections between 2020 and 2005 is shown in Figure 21. Below the areas of major change in the reservoir (to the right of CDP 8412.5) the decrease in the velocity of the reservoir produces a time shift in the 2020 seismic responses below the reservoir, resulting in the events around 1100 ms that do not reflect CO_2 saturation changes at this depth, only the time shift from CO_2 above.

There is a large, and easily measurable, change in the stacked trace amplitude associated with the reservoir caused by the changes in S_w and S_{CO_2}. In addition, there is a change in the AVO effects as seen in Figure 19. Both amplitude and AVO can be exploited to make quantitative estimates of saturation changes under certain conditions. Convolutional forward calculations using the Zoeppritz equation for both the 2005 and 2020 models provide insight into the AVO dependence on model parameters. The forward modeling creates a synthetic seismic gather from a given set of elastic parameters V_p, V_s and density as a function of depth. The full Zoeppritz equation is used to compute the acoustic to acoustic (pp) reflection coefficient $R_{pp}(\theta)$ for each angle and at each layer boundary. Synthetic seismic CDP gathers are calculated by convolving the angle-dependent reflection coefficients with a 50 Hz Ricker wavelet. The convolution model assumes plane-wave propagation across the boundaries of horizontally homogeneous layers, and takes no account of the effects of geometrical divergence, inelastic absorption, wavelet dispersion, transmission losses, mode conversions and multiple reflections. Hence, it is easier to understand intuitively than the finite-difference modeling of Figures 18–21, but demonstrates similar features.

The change in V_p, V_s, and density within the reservoir (depth between 1250 and 1275 m) is shown in Figure 22. The synthetic CDP gathers as a function of angle are shown in Figure 23a and b for 2005 and 2020, respectively. The change in reflection amplitude between 2020 and initial conditions is shown in Figure 24. The AVO response of the composite reflections from the reservoir interval shows increasing negative amplitude with offset, a typical Class 3 gas response. The negative trough (associated with the top of the reservoir) increases its magnitude with offset and is followed by a peak, also increasing with offset.

Use of AVO in fluid saturation prediction. The AVO attributes of reflections from the reservoir can be used to estimate fluid saturations under certain circumstances. AVO data can be used to estimate the acoustic and shear impedance of the reservoir [9]. When used in a time-lapse sense, these data can provide estimates of the change in water saturation and pressure within the reservoir [10].

The ability to predict changes in water saturation and pressure within a reservoir is illustrated in Figure 25. Here, the methods referenced above, and the rock-properties model derived for the North Sea sands

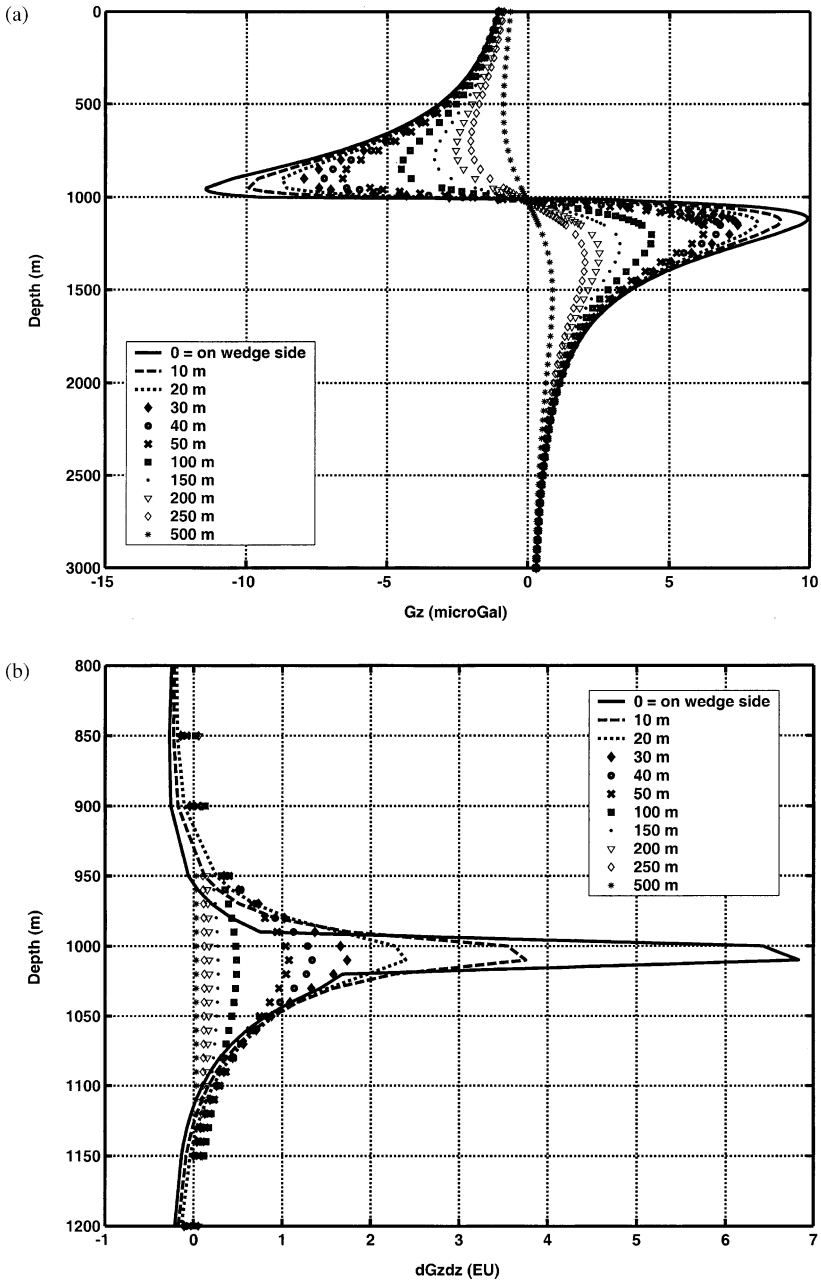

Figure 14: (a) Borehole gravity response of the model in Figure 13 as a function of distance from the wedge edge. (b) Borehole vertical gradient gravity response of the model in Figure 13 as a function of distance from the wedge edge.

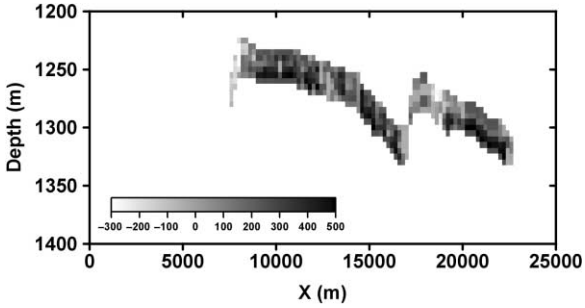

Figure 15: Change in the acoustic velocity (V_p) between 2020 and 2005 along a 2D profile extracted form the 3D model volume. The profile runs N45°E across the 3D model. Note the significant decrease in V_p associated with the increase in S_{CO_2} (Figure 16).

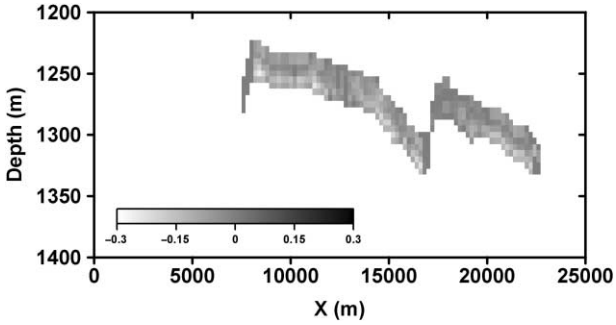

Figure 16: Change in the S_{CO_2} between 2020 and 2005.

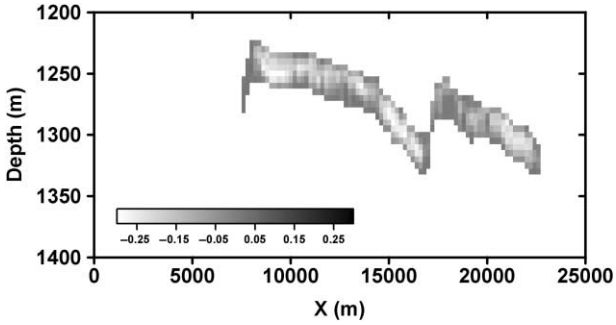

Figure 17: Change in S_w between 2020 and 2005.

of the Troll reservoir [4] is used to calculate the changes in shear and acoustic impedance of the reservoir as the water saturation and pore pressure for two cases of oil saturation as CO_2 is introduced. The first case (open circles) has initial oil and water saturation of 50%, as CO_2 is introduced it replaces water. The second case (closed circles) has an initial oil saturation of 60 and 40% water, with CO_2 replacing water. In both

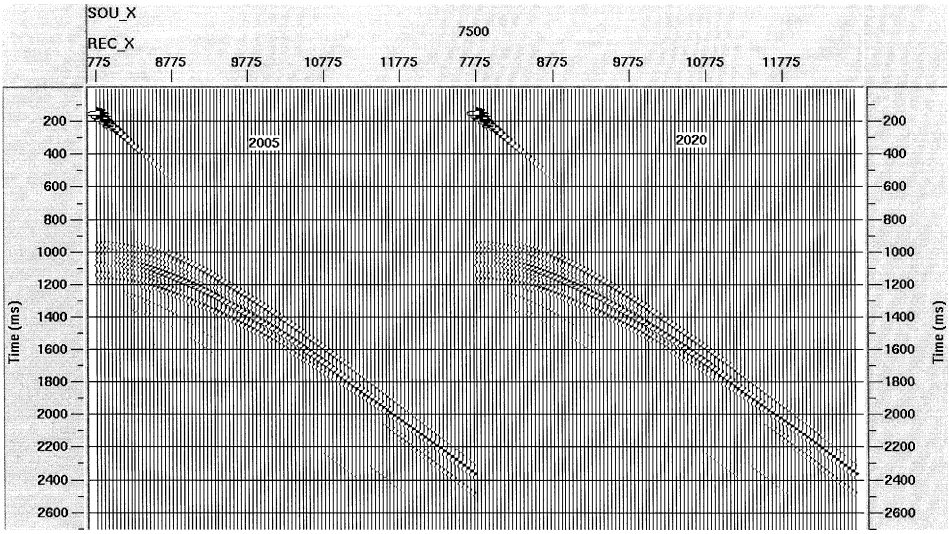

Figure 18: Seismic pressure response (shot gather) for 2005 and 2020.

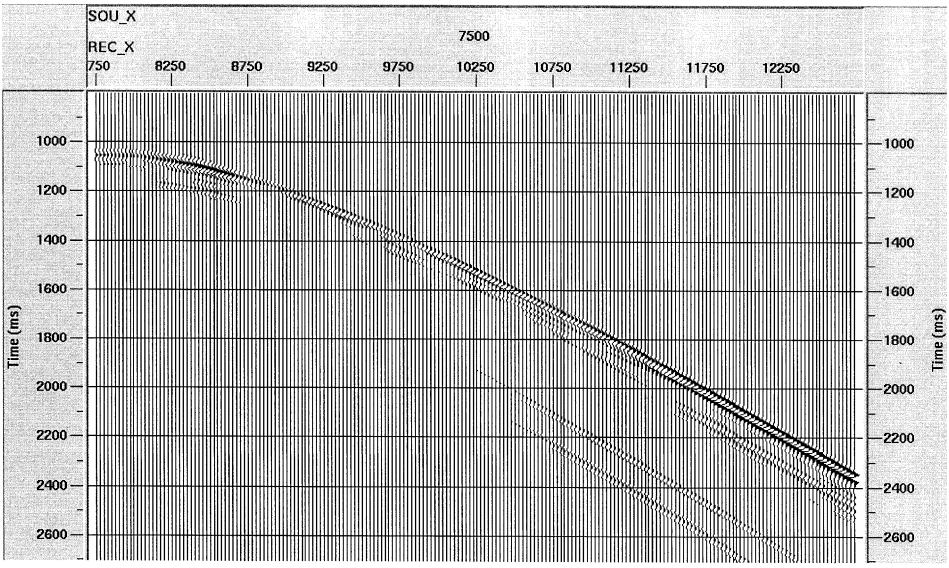

Figure 19: Change in pressure response (shot gather) between 2020 and 2005. Note amplitude change and AVO effects associated with S_w and S_{CO_2} changes in the reservoir.

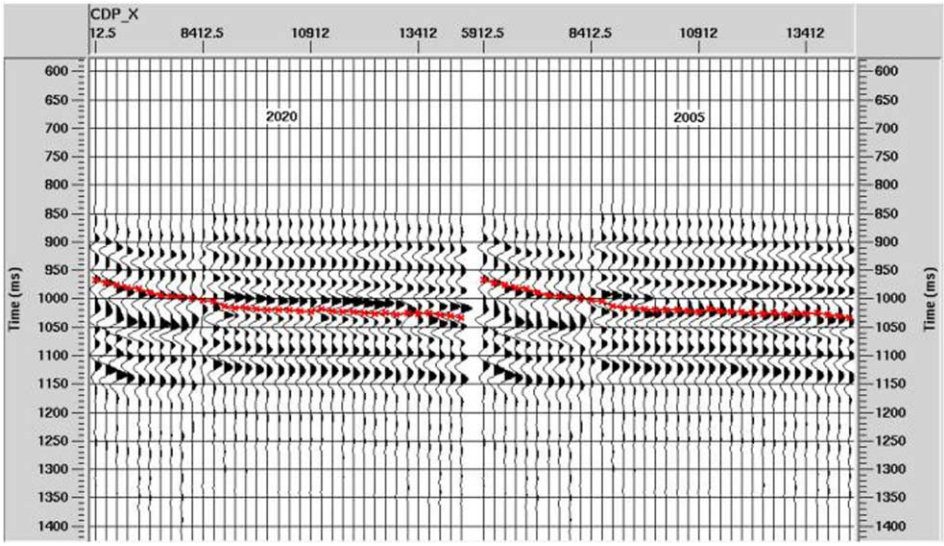

Figure 20: Stacked section for 2005 and 2020, gray line is constant time pick for reference.

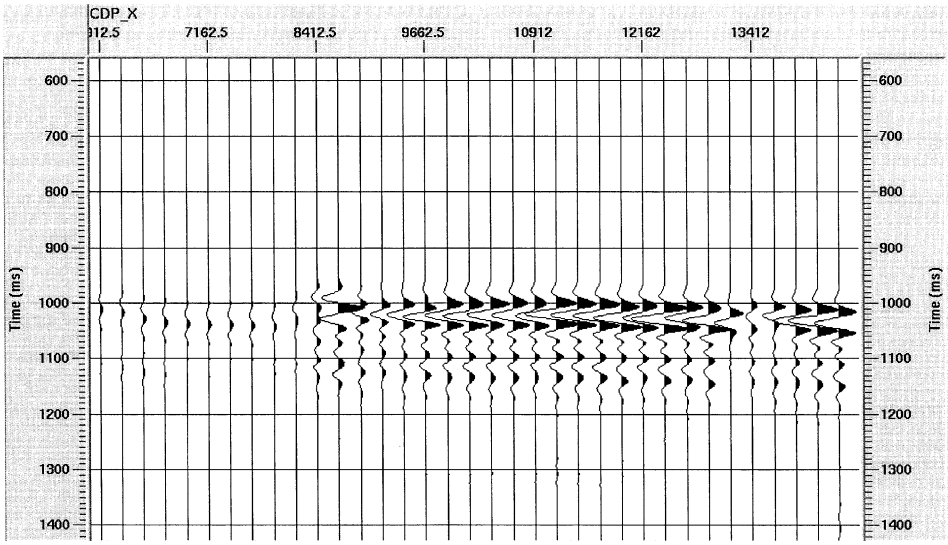

Figure 21: Change in the stacked sections between 2020 and 2005 (2020−2005).

cases S_{CO_2} ranges from 0 to 30%. Each point in the figure represents a unique value of S_w and S_{CO_2} with the oil saturation held fixed at either 50 or 60%. S_{CO_2} values increase in increments of 0.015% from right to left on the figure, and pore pressure increases and decreases (indicated by arrows) from the reference pressure of 24.24 MPa by increments of 0.7 MPa.

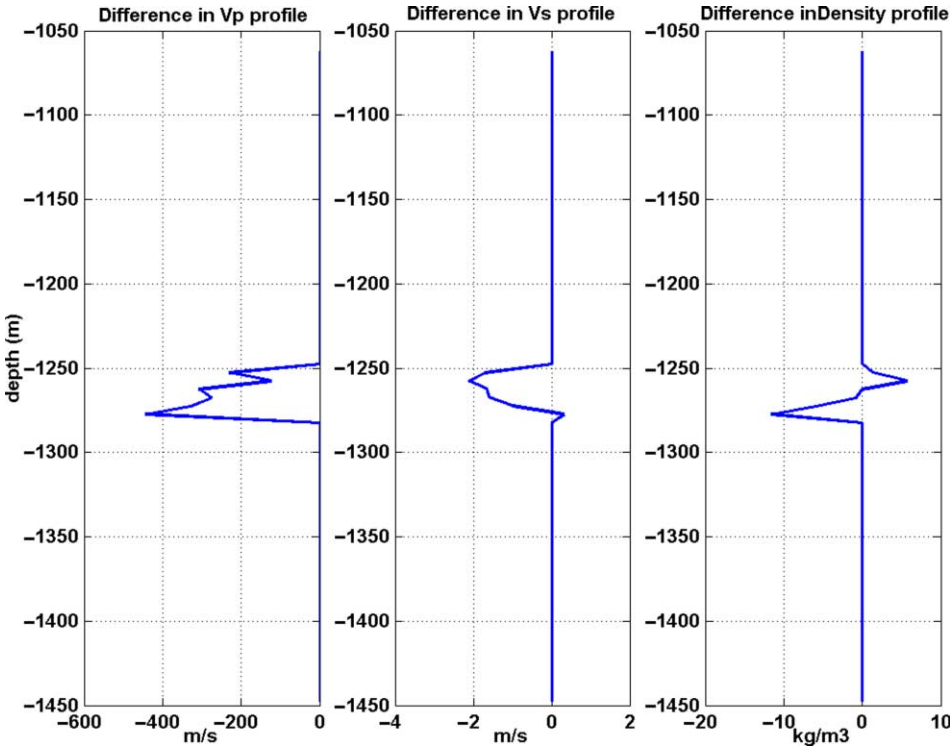

Figure 22: Difference in V_p, V_s, and density profiles between 2020 and 2005 for the Schrader Bluff model at the center of maximum CO_2 saturation increase.

Figure 25 illustrates four important points: (1) if the oil saturation is known, the changes in shear and acoustic impedance of the reservoir can determine the change in pressure and CO_2 saturation, (2) the changes in the shear impedance required to make the estimates is quite small and would require extremely good shear data, (3) an uncertainty in the oil saturation level of 10% in this example has only a small effect on the estimated values of changes in S_{CO_2} and almost no effect on the estimates of pressure change, (4) in this model, fluid saturation changes affect mostly the acoustic impedance, while fluid pressure changes affect mostly the shear impedance. In this example the change in the acoustic impedance alone could provide estimates of the change of S_{CO_2} even if the pressure changes could not be estimated due to insufficient accuracy on the shear impedance estimates.

An uncertainty on the value of oil saturation has limited effects in these calculations because of the relative similarity of the bulk modulus and density of oil, compared to water, when either is compared to CO_2. The situation is significantly different if there is hydrocarbon gas (such as methane) in the reservoir. In this case (due to the extreme differences between the properties of methane and water) even a small uncertainty in the hydrocarbon gas saturation leads to very large uncertainties in the estimated values of pressure and CO_2 saturation changes, making this technique essentially unusable unless an independent estimate of water saturation or gas saturation can be obtained from other methods [3].

While estimation of changes in fluid saturation using AVO is complicated by the multiple fluid components in oil or gas reservoir, the situation is simpler in a brine reservoir. For cases where CO_2 is injected into

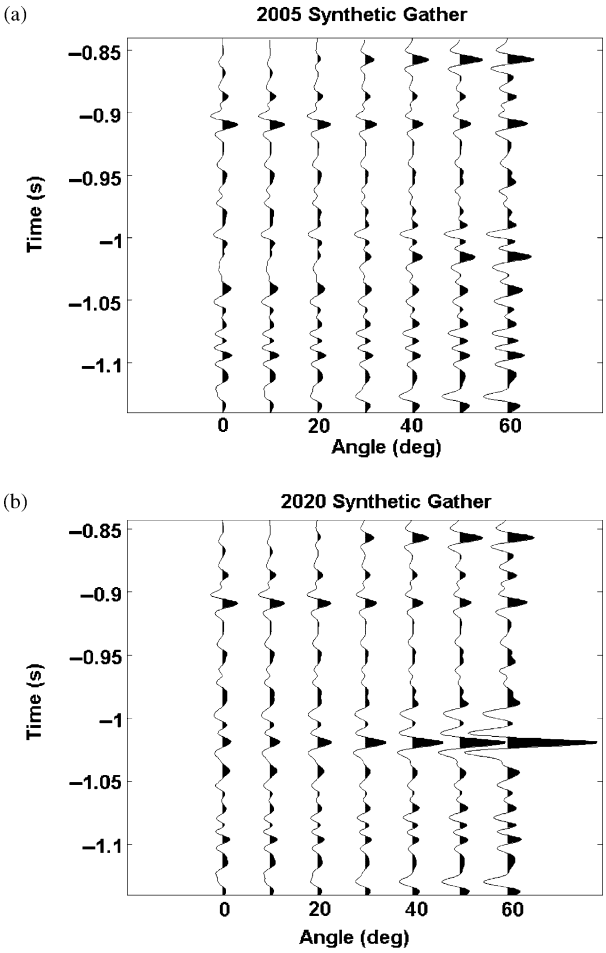

Figure 23: Synthetic gather for (a) 2005 and (b) 2020.

a brine reservoir, there are only two fluid components (brine and CO_2) and the added constraint that their saturations levels sum to one. In this case, AVO information can more easily be used to estimate the level of CO_2 in the reservoir. The following example illustrates this process. An unconsolidated North Sea sand of the Troll reservoir [4] encased in shale is assumed to contain 50% brine and 50% CO_2 as the reference point for these calculations. Pressure and temperature are such that the CO_2 is in the liquid state. The values of CO_2 (and hence water) saturation and pore pressure are varied about this starting point and the acoustic and shear velocities as well as density are calculated.

The reflection coefficient at the top of the reservoir can be approximated [11] by

$$R(\theta) \approx A + B\sin^2(\theta) + C\sin^2(\theta)\tan^2(\theta) \tag{1}$$

where θ is the average of the reflection and transmission angle for a plane wave hitting the interface. The constants A and B are referred to as the intercept and slope, respectively, in the AVO literature.

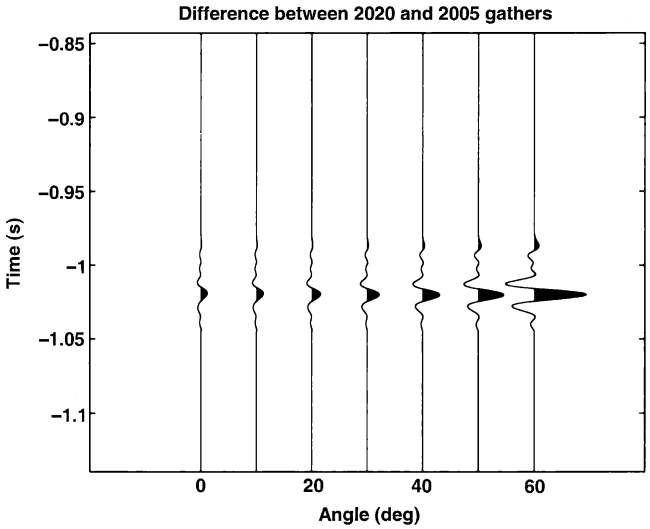

Figure 24: Difference between 2020 and 2005 gathers.

The constants A, B and C are functions of the velocity and density of the media on either side of the reflecting interface and are given by

$$A = 1/2(\Delta V_p/\langle V_p\rangle + \Delta\rho/\langle\rho\rangle) \tag{2}$$

$$B = 1/2(\Delta V_p/\langle V_p\rangle - 2(\langle V_s\rangle/\langle V_p\rangle)^2(2\Delta V_s/\langle V_s\rangle + \Delta\rho/\langle\rho\rangle)) \tag{3}$$

$$C = 1/2(\Delta V_p/\langle V_p\rangle) \tag{4}$$

where ΔV_p is the change in acoustic velocity across the interface and $\langle V_p\rangle$ is the average acoustic velocity across the interface, ΔV_s, $\langle V_s\rangle$, $\Delta\rho$, and $\langle\rho\rangle$ are changes and averages for shear velocity and density, respectively. If time-lapse seismic data is acquired, and A and B are estimated from the AVO data and used to calculate ΔA and ΔB, the associated ΔS_{CO_2} and ΔP_p can be estimated from model-based calculations such as illustrated in Figure 26. This example illustrates a theoretical case without noise in the seismic data; in practice estimation of the "curvature", C, is the most difficult. Extremely high signal-to-noise (S/N) seismic data would be required even for estimates of B accurate enough to make pressure change estimates. Even with poor estimates of B changes, in S_{CO_2} could be estimated from the changes in the zero offset impedance (A) because the contours in Figure 26a are nearly orthogonal to the ΔA axis.

Electromagnetic modeling

The electrical resistivity of reservoir rocks is highly sensitive to changes in water saturation. This can be seen from Archie's Law [12], which is commonly used to describe the electrical resistivity of sedimentary rocks as a function of water saturation, porosity, and pore fluid resistivity. Figure 27 shows the rock bulk resistivity (in Ωm) as a function of gas saturation ($S_g = 1 - S_w$) for a reservoir with brine resistivity equivalent to sea water ($\rho_{brine} = 0.33\,\Omega$m) with 25% porosity. All petroleum fluids (oil, condensate, and hydrocarbon gas) as well as CO_2 are electrically resistive, hence the relation shown in Figure 27 is appropriate for any combination of oil, hydrocarbon gas, condensate, or CO_2.

The bulk resistivity in Figure 27 is plotted on a log scale to span the large range of resistivity values as a function of the gas saturation (S_g). This high sensitivity to water saturation in a reservoir can be exploited by electromagnetic (EM) techniques, where the response is a function of the rock bulk electrical resistivity. Of all the possible combination of EM sources and measured EM fields, one system combines both relative ease of deployment with high sensitivity to reservoirs of petroleum scale and depth. This technique uses a grounded electric dipole that is energized with an alternating current at a given frequency to produce time

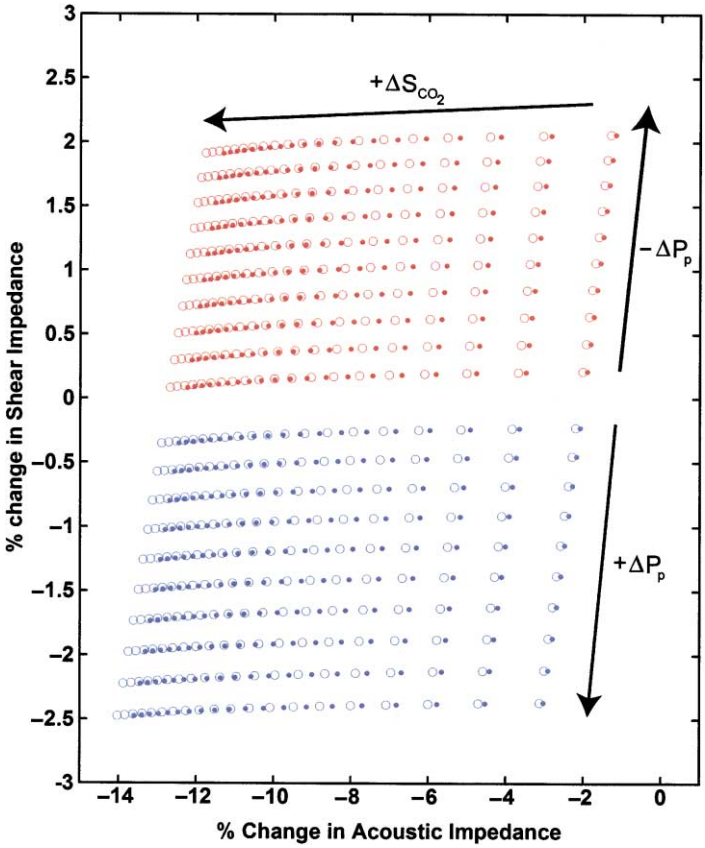

Figure 25: Changes in pore pressure (ΔP_p) and CO_2 saturation (ΔS_{CO_2}) as a function of changes in the shear and acoustic impedance of the reservoir. Open circles represent oil saturation of 50% with CO_2 replacing water. Filled dots represent oil saturation of 60% with CO_2 replacing water. Initial pore pressure is 25.24 MPa, initial S_{CO_2} is 0%. S_{CO_2} increments are 0.015 and pressure increments are 0.7 MPa.

varying electric and magnetic fields that can be measured on the earth's surface. The electric dipole can consist of two steel electrodes (1 m^2 plates or sections of drill pipe) buried at a shallow depth (1–10 m) separated by 100 m and connected by cable to a low-power generator (a portable 5000 W generator is sufficient). The measured data would consist of the electric field at a given separation from the transmitter acquired on the surface or within the near surface.

To simulate such an EM system we have calculated the electric field on the surface of the Schrader Bluff model using 100 m electric dipoles operating at 1 Hz with measurements of the resulting electric field at a separation of 2 km in-line with the transmitting dipole. Figure 28 shows the amplitude of the generated EM field at 2 km separation and 1 Hz together with the natural background electric field generated from worldwide thunderstorms and pulsations in the earth's ionosphere. Figure 28 shows that the generated electric field for the Schrader Bluff model, using only a small portable generator (producing a 10 A current in the source dipole) is an order of magnitude above the background electric field (noise) at the operating frequency of 1 Hz. This means that synchronous detection of the signal combined with stacking can recover signal variations to better than 1%.

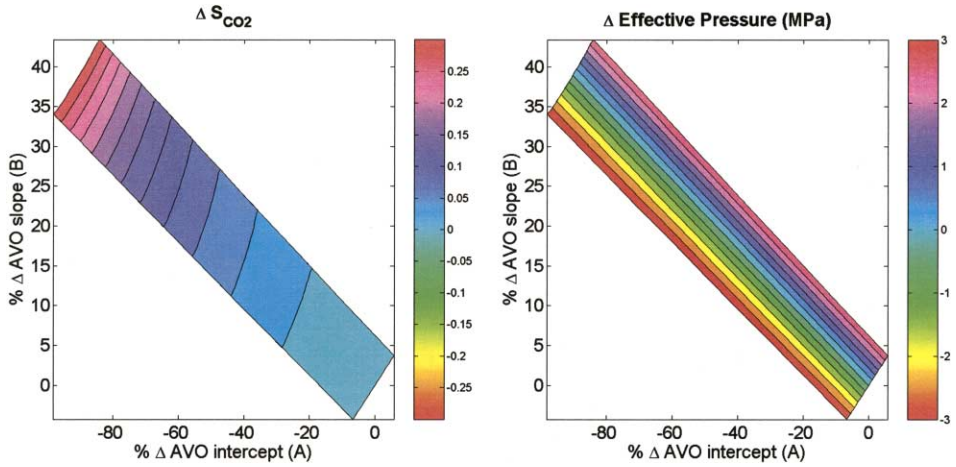

Figure 26: Contours of the change in CO_2 saturation (left panel) and effective pressure (lithostatic − pore pressure) (right panel) as function of the change in the AVO intercept (A) and slope (B) for an unconsolidated sand surrounded by shale.

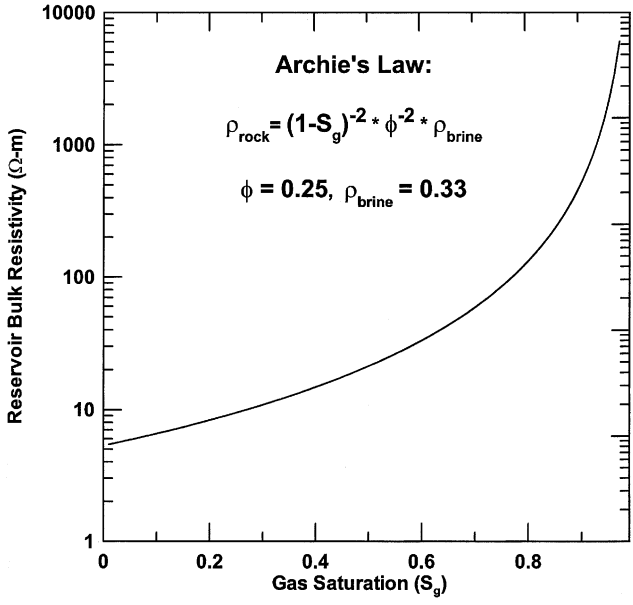

Figure 27: Reservoir bulk resistivity as a function of gas saturation (S_g). Porosity = 25%.

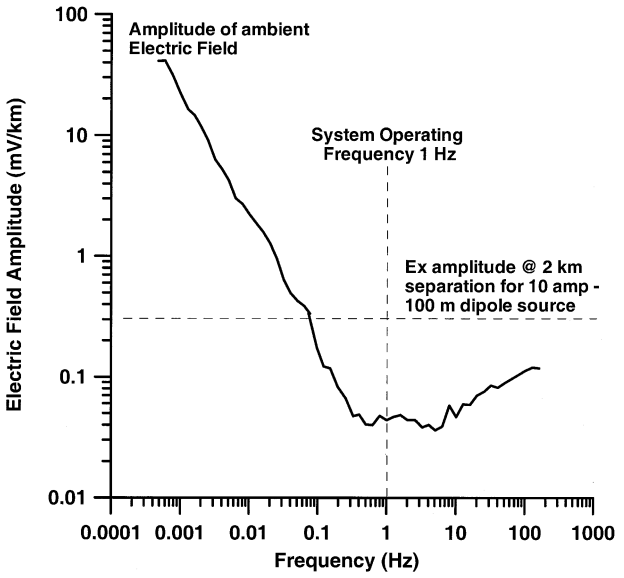

Figure 28: Amplitude of naturally occurring electric field as a function of frequency [34] that would be considered noise to that EM system considered here for monitoring, shown as solid curve. The horizontal dotted line represents the signal amplitude at a source–receiver separation of 2 km at an operating frequency of 1 Hz for a 100 m electric dipole energized with 10 A of current.

Figure 29 shows the net change in water saturation within the reservoir (vertically integrated ΔS_w) between 2020 and initial conditions. The change in the electric field amplitude for the same interval is overlaid as black contour lines, with peak-to-peak amplitude of 1.2%. There is a direct one-to-one correspondence with the change in S_w and the change in the electric field amplitude. While this signal level is low, it can be measured given the S/N ratio of the data (Figure 28). Although this represents a potential low-cost monitoring technique it is best suited for CO_2–brine systems where there is a one-to-one correlation between the change in S_w and the change in S_{CO_2} (since $S_w + S_{CO_2} = 1$).

In a petroleum reservoir such as Schrader Bluff, the presence of hydrocarbons as additional fluids eliminates the one-to-one correlation between changes in S_w and changes in S_{CO_2}. This is illustrated in Figure 30 where the same changes in electric field amplitude are overlaid on the net change in the CO_2 saturation within the reservoir between 2020 and initial conditions. In this case, we see that the correlation between changes in S_{CO_2} and changes in the electric field amplitude are not as good as seen between changes in S_w and the electric field data.

This type of EM technique has not yet been employed as a monitoring tool within the petroleum industry. However, EM technology is currently the subject of a significant upsurge in industry interest. Several commercial contractors are now offering this technique as a survey tool, most notably, in the offshore environment where marine EM is used as an exploration tool [13]. The equipment and service providers exist to apply this technique for monitoring in the future.

On-Shore Saline Aquifer—Frio Formation, Texas

Brine-bearing formations that are below and hydrologically separated from potable water reservoirs above have been widely recognized as having high potential for CO_2 storage. One of the most promising sites is the Frio Formation in Texas, which has been chosen as a field demonstration site as part of the US DOE and

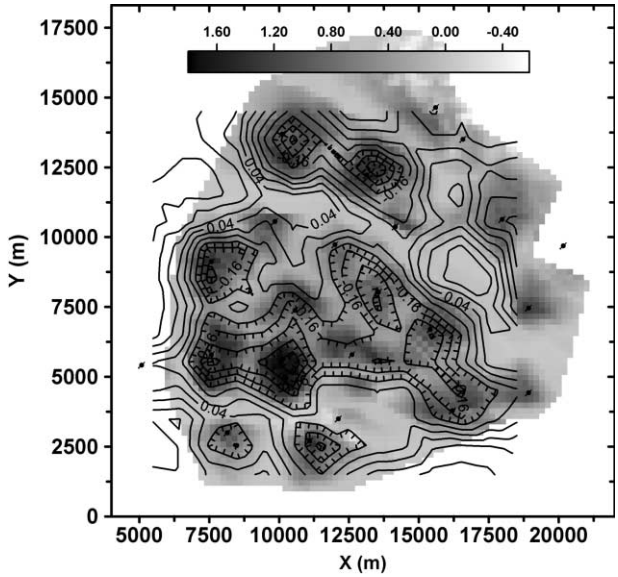

Figure 29: Shaded color map of the net change in water saturation over the vertical interval of the reservoir between 2020 and initial conditions. The change in the amplitude of the electric field from an electric dipole source at a separation of 2 km is overlaid as black contours. The peak-to-peak change in electric field amplitude is 1.2%. Note the direct correlation between decreases in the electric field amplitude and increases in water saturation (decreased electric resistivity of the reservoir). Locations of injection wells are shown by black circles with arrows through them.

National Energy Technology Laboratory (NETL) sponsored GeoSeq project. The test demonstration project has four main goals: (1) demonstrate that CO_2 can be injected into a saline formation without adverse health, safety, or environmental effects, (2) determine the subsurface location and distribution of the injected CO_2 plume, (3) demonstrate an understanding of the conceptual models, and (4) develop experience necessary for the success of future large-scale CO_2 injection experiments [14].

The South Liberty pilot test site lies on the south side of a salt dome (Figures 31 and 32). The injection target is the Frio Formation; strongly compartmentalized by a pattern of high-angle faults radiating from the salt dome and associated cross faults. The structure and fault boundaries used for modeling are based on structure and fault patterns mapped from 3D seismic data. This structural interpretation has a 440 m-wide compartment with fault boundaries on the northwest, northeast, and southeast. A fault boundary in the southwest side of the compartment was not imaged within the seismic volume, so the closure on this side is unknown and is considered as a variable in the modeling experiment. Within the compartment, strata are tilted off the salt dome. At the injection well, the top of the Frio Formation is at about 1500 m depth, strikes N70°W, and dips 15° toward the southwest. Stratigraphy employed for the flow modeling focuses on the selected injection interval, a 12-m thick high-porosity, high-permeability sandstone referred to as the C sand, which is separated into upper and lower halves by a thin (0.3 m) shale layer. The section below the thin shale, an upward-coarsening sand, is the actual injection target. Locally extensive shale deposited within the Frio during cycle-bounding flooding events form sealed boundaries at the top and bottom of the C sand. The thick regionally extensive shale of the Anahuac Formation overlies the Frio Formation and provides an additional impermeable boundary isolating CO_2 from the land surface. The regional geothermal gradient is taken to be 32.6 °C/1000 m [15]. For Frio water chemistry at these depths, reasonable values are

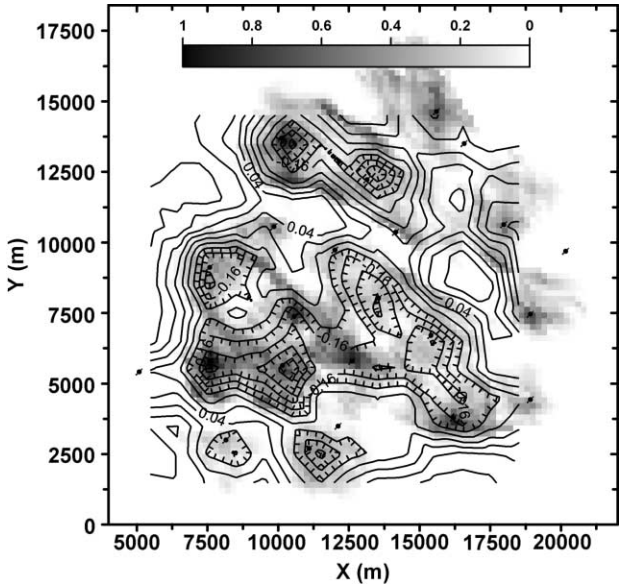

Figure 30: Shaded color map of the net change in CO_2 saturation (ΔS_{CO_2}) over the vertical interval of the reservoir between 2020 and initial conditions. The change in the amplitude of the electric field from an electric dipole source at a separation of 2 km is overlaid as black contours. The peak-to-peak change in electric field amplitude is 1.2%. Location of injection wells are shown by black circles with arrows through them.

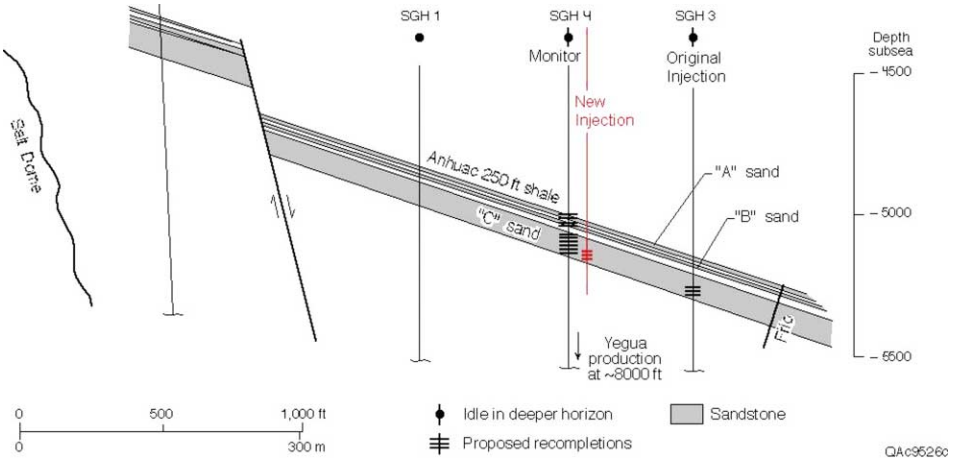

Figure 31: Schematic cross-section of the Frio Formation at the South Liberty pilot test site, Texas.

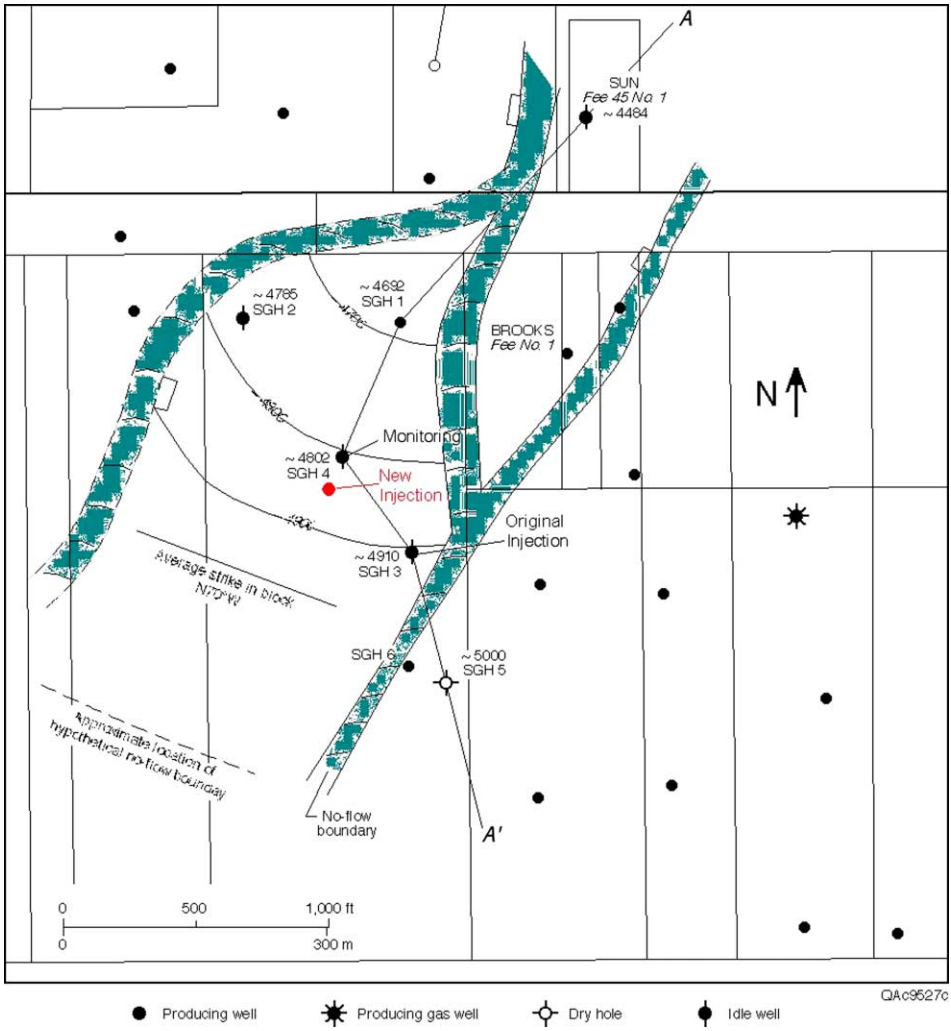

Figure 32: Schematic plan view of the South Liberty pilot test site. The shaded bands show sub-vertical faults that are assumed to act as impermeable barriers to fluid flow.

TDS 100,000 ppm, Na 35,000 ppm and Cl 45,000 ppm [16]; these values affect the fluid resistivities discussed below. The injection interval is non-productive of hydrocarbons.

CO_2 will be trucked to the site and injected into the high-permeability C sand within the upper Frio formation. There will be a series of field monitoring experiments before, during, and after CO_2 injection. These experiments will test effectiveness of a spectrum of CO_2 monitoring techniques and compare the results to validate the methods. Injection will be completed within 15–20 days, followed by up to a year of monitoring and assessment. There is one monitoring well, located about 30 m up-dip of the injection well (Figures 31 and 32).

Based on the geological setting of fluvial/deltaic Frio Formation, a 3D stochastic model of the C sand was created for fluid flow and transport modeling using a two-phase (liquid, gas), three-component (water, salt, and CO_2) system in the pressure/temperature regime above the critical point of CO_2 ($P = 73.8$ bars, $T = 31\,^{\circ}C$) [18]. When CO_2 is injected in a supercritical state it has a much lower density and viscosity than the liquid brine it replaces, making buoyancy flow a potentially important effect. The model is bounded above and below by closed boundaries, which represent continuous shale. Three of the four lateral boundaries are closed to represent the edges of the fault block. CO_2 is injected at a rate of 250 metric tons per day (2.9 kg/s) for a period of 20 days, and then the system is monitored for an additional year. Initial formation conditions are $P = 150$ bars, $T = 64\,^{\circ}C$ and TDS = 100,000 ppm. Under these conditions, supercritical CO_2 has a density of 565 kg/m^3 and a viscosity of 4.3×10^{-5} Pa s. In the reservoir, about 15% of the CO_2 dissolves in the brine, with the remainder forming an immiscible gas-like phase.

During the 20-day injection period, flow simulations show the distribution of CO_2 is nearly radially symmetric around the injection well (Figure 33). The plume arrives at the monitoring well in 2–3 days. After injection ends, the modeled plume begins to spread and it does not take long (approximately 30 days) for gas saturation to decrease to the residual value, making the plume essentially immobile.

During this test, less than 5000 tons of CO_2 will be injected into a 6 m thick sand unit at a depth of 1500 m. As such, it is a good limiting case for detection and resolving capabilities of geophysical monitoring techniques. A flow simulation model of the injection target was created using geo-statistical realizations of the sand shale distributions based on log data. Log data were used to construct rock-properties models that relate the reservoir parameters to geophysical parameters. These relations were used to convert the flow simulation model to geophysical models.

Streaming potential measurements
Fluid flow within a porous media can produce an electrical potential due to the separation of ions across flow boundaries. This phenomenon is the basis of the Streaming Potential (SP) method. SP has been used in geothermal exploration [19], in earthquake studies [20,21]), and in engineering applications [22–24]. Early model studies were based on polarized spheres or line dipole current sources. These techniques provided very little information about the nature of the primary sources. Marshall and Madden [25] discussed source mechanisms in detail and provided a technique for the solution of coupled flows that incorporated the primary driving potential. Sill [26] presented an alternative method for the solution of coupled flow problems that explicitly models both the primary flow and the induced secondary electric potential.

The measurement of the SP generated electric fields is a relatively simple and low cost measurement. The ease of the measurement coupled with the fact that the data is generated directly by the flow phenomena suggests a potential technique for low-cost, low-resolution monitoring.

The gradient of the electric potential (electric field) produced at a flow boundary by the SP is given by:

$$\nabla\phi = L\frac{\Gamma\mu}{k\sigma}$$

where L is the so-called "coupling coefficient", Γ the primary fluid flux, related to the pressure gradient by Darcy's Law, k the solution dielectric constant, σ the bulk conductivity of the rock, and μ the fluid viscosity.

A review of the literature showed that there was very little data on the coupling coefficient, L, for flow of CO_2 within sedimentary rocks. This led to a program of laboratory studies to measure this parameter. In the following sections we describe the laboratory and the numerical modeling studies.

SP laboratory studies. Laboratory studies were done for the SP due to CO_2 injection in Berea sandstone (Lang Stone, Columbus, OH). These are the first such measurements for CO_2 to our knowledge. The testing device held a 127 mm long core of 25 mm diameter (Figure 34). Tests were run on two different rock samples. Each sample was saturated prior to testing under vacuum for a period no less than 1 day. The pore

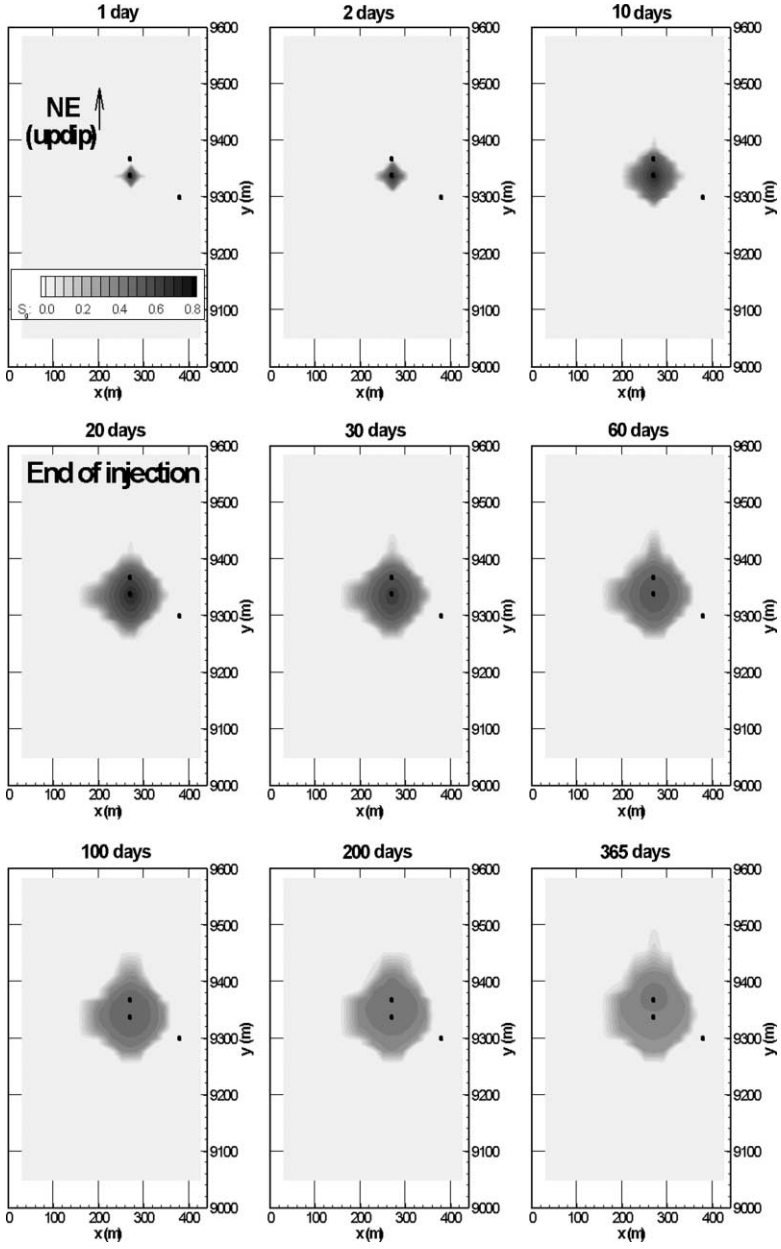

Figure 33: Plan view of gas saturation (S_{CO_2}) distribution at the top of the injection interval within the C sand, for a series of times during and after CO_2 injection. The three black dots show the locations of well SGH-3, well SGH-4, and the new injection well (see Figures 31 and 32).

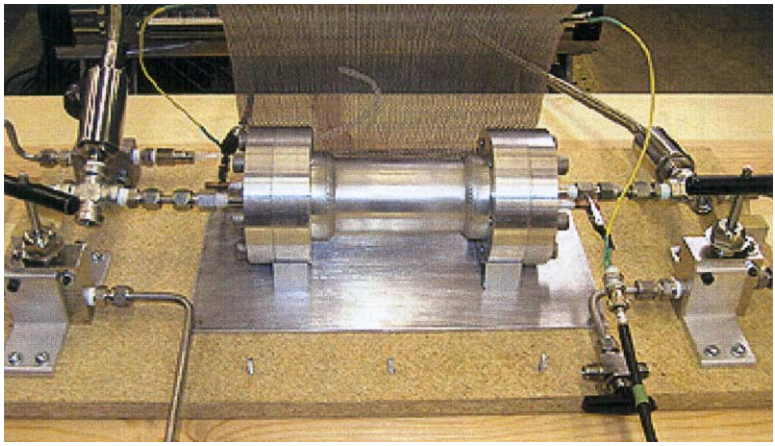

Figure 34: Testing device containing Berea sandstone core. Sample is 127 mm long and 25 mm diameter.

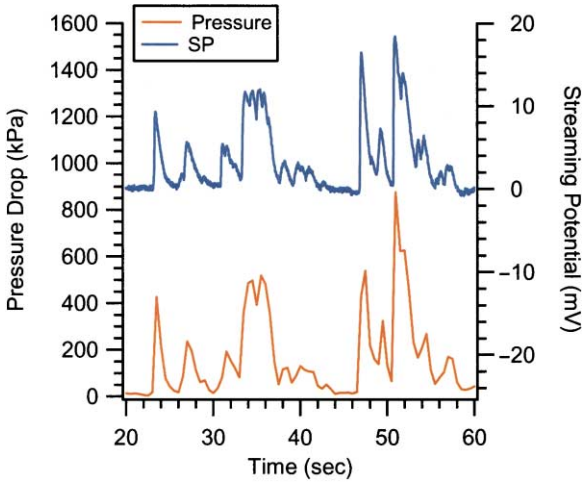

Figure 35: Streaming potential and pressure changes as a function of time as CO_2 is injected into the core sample.

fluid for initial saturation was Berkeley tap water, tested to have a resistivity of 125 Ω m. The coupling coefficient for the rock/water case was determined both before and after each CO_2 flood of two samples using a low-pressure static head method. Between these tests, liquid CO_2 was flowed over each sample. Test 1 allowed liquid CO_2 to flow through the sample for $1\frac{1}{2}$ h, while test 2 lasted 1 h. Figure 35 illustrates that the observed potentials and applied pressure changes correlated well throughout the testing. For these low-pressure tests, results indicate linear correlation of applied pressure and observed potential, as illustrated in Figure 36. When liquid CO_2 was applied to the sample, the water in the sample pore space was displaced, while reacting with the CO_2 to form carbonic acid. The coupling coefficient evolved over time in response to the mixing and displacing of the pore water. Figure 37 shows the coupling coefficient evolution of both tests

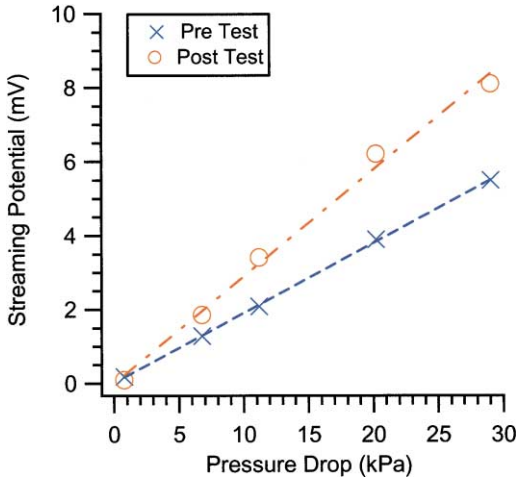

Figure 36: Results for static head testing to determine water-only coupling coefficient both prior to and following CO_2 injection test 2. Resistivity of pore fluid was 125 Ω m. Slope of line indicates coupling coefficients of 20 mV/0.1 MPa (pre) and 30 mV/0.1 MPa (post).

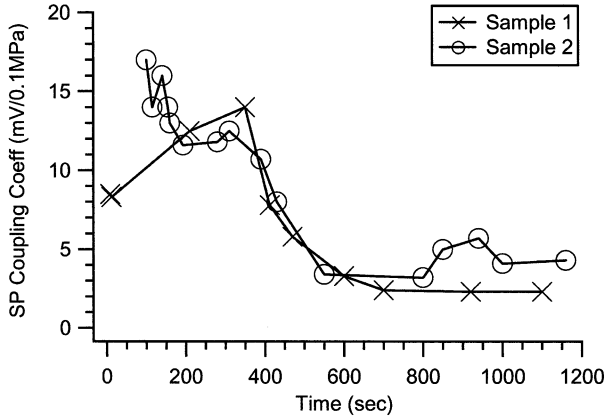

Figure 37: Coupling coefficients as a function of time for the first 20 min of CO_2 injection for samples 1 and 2. Coupling coefficient values were steady for times greater than 700 s, and remained steady throughout the remaining testing time.

for the 20 min following CO_2 injection. The results of the test are summarized in Table 1. As the CO_2 displaced the water the coupling coefficient decreased. On average, the coupling coefficients observed for steady CO_2 flow is about 10 times lower than for water flow in the same sample. Since the liquid CO_2 coupling coefficient is smaller than that of water, the most effective way to monitor spatial variation in injected CO_2 flow is to monitor the progressing CO_2/water front, where the coupling coefficient is largest.

SP modeling. In order to determine the magnitude of the SP response a 2D numerical model based on the geology and configuration of the Liberty Field CO_2 injection test was used. The model consists of a 10 m

thick sand unit at a depth of 1,500 m embedded in shale. The resistivity of the sand unit is 2 Ω m, while the resistivity of surrounding shale is 1 Ω m. The flow rate of CO_2 is 350 kg/s; the viscosity of CO_2 is 0.073×10^{-3} Pa s and the density of CO_2 is 788 kg/m^3 at a temperature of 70 °C and a pressure of 30 MPa. The model is shown in Figure 38a. The 2D algorithm developed by Sill [26] was used. This algorithm assumes the fluid sources to be a line perpendicular to the geologic variation at steady state conditions (constant flow of a single-phase fluid).

TABLE 1
SUMMARY OF COUPLING COEFFICIENT RESULTS

	Pre-test (water)	**During (CO_2)**	**Post-test (water)**
Sample 1	45	2.5	15
Sample 2	20	3.5	30

All units are in mV/0.1 MPa.

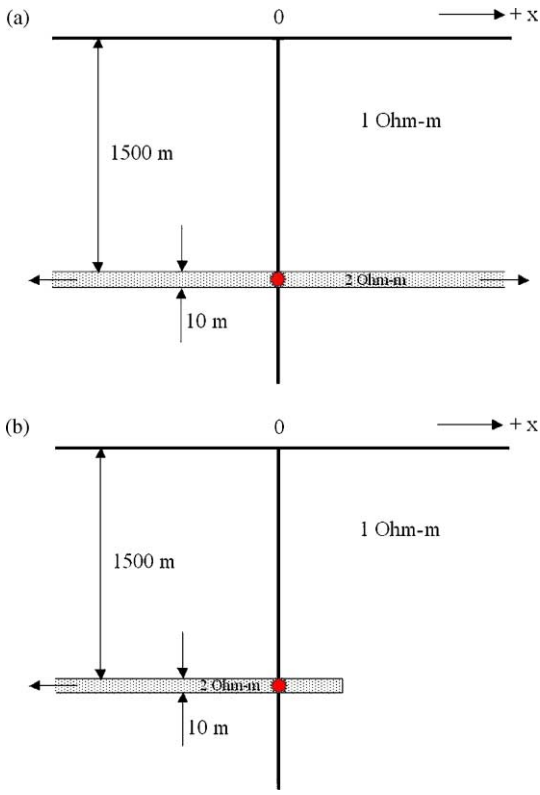

Figure 38: (a) Continuous layer model simulating the Liberty Field geology: 10 m thick sand layer at a depth of 1500 m. (b) Layer truncated at +300 m in x.

Figure 39a shows the pressure distribution for the model in Figure 38a with the associated electric potential shown in Figure 39b. In general, SP noise sources are on the order of a few to 10 s of mV although this number is highly site specific. SP signals over 10 mV are considered large.

The model shown in Figure 38b has the same parameters as the model in Figure 38a, except that the sand layer is terminated at +300 m. Comparison of results from these two models give an indication of the ability of SP surface measurements to resolve lateral variations in the subsurface flow of CO_2. The largest effect of the layer truncation is to concentrate the flow onto the left side of the model, increasing the flux and the pressure gradient there, thus increasing the magnitude of the SP observed at the surface. The truncation of the layer also introduces an asymmetry in the surface SP response (solid curve in Figure 40). The response is 10 mV higher on the truncated side than on the continuous side. The ability to differentiate this spatial variation in the signal will depend on the background noise level in the electric fields on the surface.

The effects of layer depth on the SP response are shown in Figure 41. A 100 m thick sand layer (properties taken from the Liberty test site) is placed at depths of 500, 1000, 1500, and 2000 m, respectively. The deeper the sand layer is the smaller is the signal amplitude on the surface.

Another aspect of interest is the effects of CO_2 flow rate on the SP response. Figure 42 illustrates that the SP response increases with CO_2 flow rate. The model used in this figure has a 100 m thick layer at a depth of 1000 m; all other parameters were the same as previous models. The flow rates used were 440, 293, and 40 L/s m, respectively.

To study the relationship between the thickness of the layer and the SP response models with 10, 30, 100, and 200 m thick sand layer at the depth of 1000 m were run; all other parameters were unchanged. Figure 43 shows that the amplitude of the SP response is inversely proportional to the thickness of the layer. The 10 m thick layer produces the largest response. The thinnest layers produce the largest response because the SP response is linearly proportional to the fluid flux, so that for a given injection rate, the thinner layers have a higher fluid flux.

Figure 44 illustrates how the SP response depends on the coupling coefficient L. The Liberty Field injection target is a 10 m thick layer at 1500 m depth with a lateral extent of 500–600 m. Its permeability is 150 milliDarcies, the flow rate is 4 L/s, and the viscosity of CO_2 is 73 μPa s. The model was run for three different values: 15 mV/atm (0.148 V/MPa), 57 mV/atm (0.5625 V/MPa), and 100 mV/atm (0.9869 V/MPa) representing a linear progression from potable water ($L = 15$) to resistive benzene ($L = 100$). Figure 44 shows linear dependence between the cross-coupling coefficient and the SP response.

Gravity modeling

In order to set some limits on the size and depths of CO_2 plumes that can be detected and resolved by surface gravity measurements, a wedge model of 240 m radius at the depth of 1000 and 2000 m was considered. The rock parameters were taken as general onshore Texas values of density. The surrounding shale was modeled having a density of 2240 kg/m^3 with the sand layer having 20% porosity and being brine saturated with a density of 2280 kg/m^3. The 3D wedge of CO_2 saturated sand was considered to be 100% saturated with CO_2, which resulted in a density of 2200 kg/m^3 for the wedge.

Figure 45 shows three surface response curves of the vertical component of the gravity field for the top of the wedge at 2000 m depth. The radius of the wedge is 240 m. The simulation was run for 100, 50, and 30 m thick wedges. A reasonable number for land gravity sensitivity levels is 2 μGal. For this depth, even the response of the 100 m thick wedge is below this level. This wedge (with thickness of 100 m) contains the equivalent amount of CO_2 produced by a 1000 MW US coal fired power plant in 41 days. Since the response of the 100 m thick wedge is just below the 2 μGal level, this indicates that amounts larger than 41 days production could be detected but not resolved.

A second set of models with the wedge at 1000 m depth were run; their responses are shown in Figure 46. With the CO_2 plume at 1000 m, both the 50 and 100 m thick volumes are detectable. The observed gravity response for the 100 m wedge is large enough to be resolved to some degree. Our conclusions to date are that gravity will most likely only be a useful monitoring technique for accumulations of CO_2 with depths on

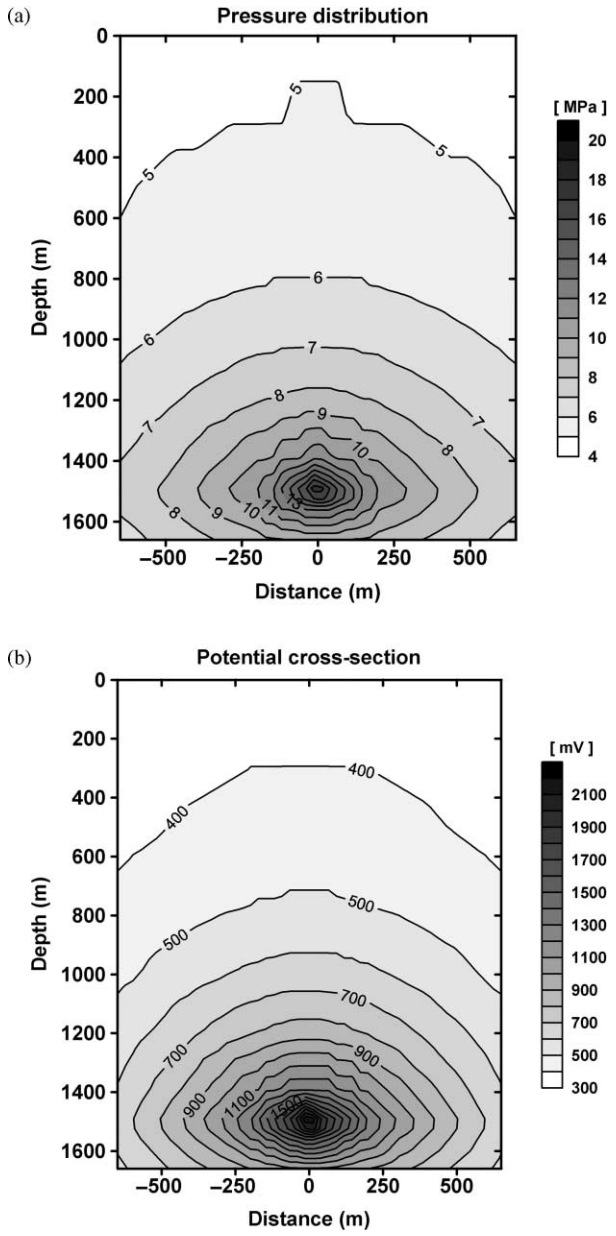

Figure 39: (a) Pressure distribution for the model from Figure 38a. (b) Electric potential cross-section for model in Figure 38a with coupling coefficient, $L = -15\,\mathrm{mV/atm}$.

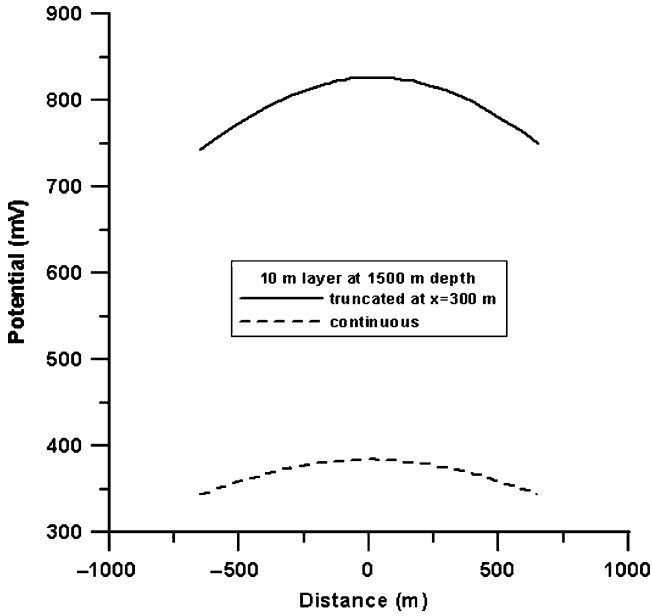

Figure 40: Surface SP response for models shown in Figure 38. Dash curve is for continuous layer; solid curve is for the truncated layer.

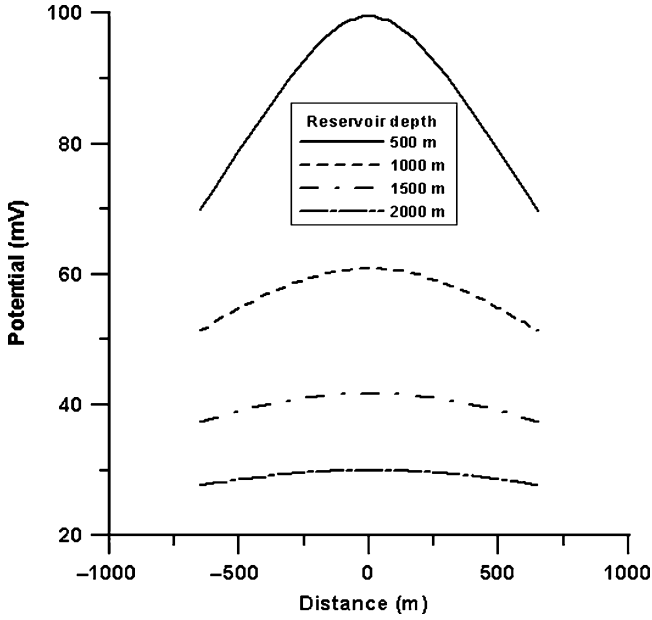

Figure 41: SP response for 100 m thick sand layer at the depth of 500, 1000, 1500, and 2000 m.

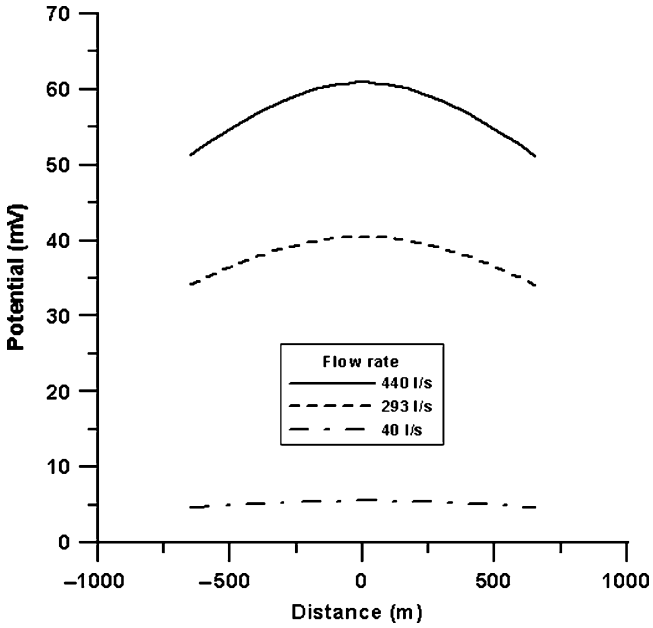

Figure 42: SP response for 100 m thick sand layer at the depth of 1000 m for the flow rate of 440, 293, and 40 L/s m.

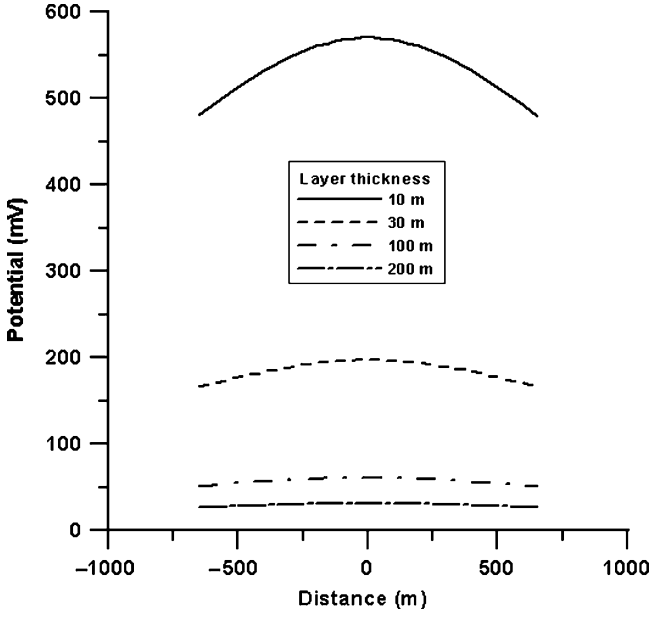

Figure 43: SP response of the 10, 30, 100, and 200 m thick sand layer at the depth of 1000 m.

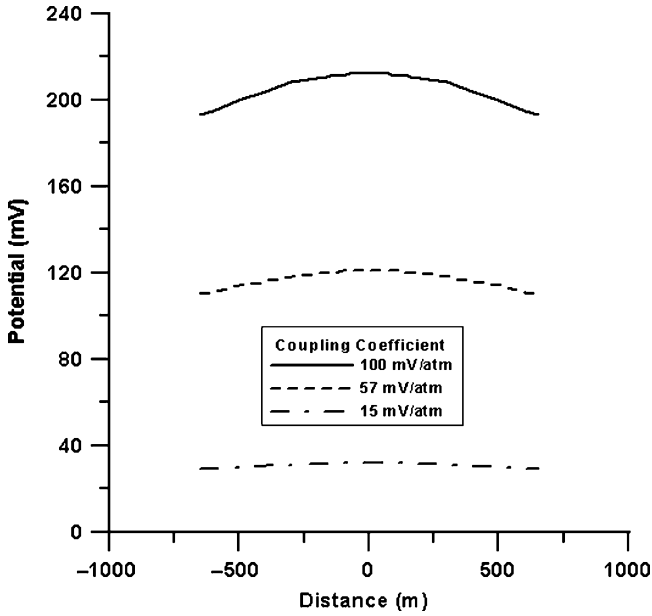

Figure 44: SP response of the Liberty Field reservoir for the coupling coefficient of 15, 57, and 100 mV/atm.

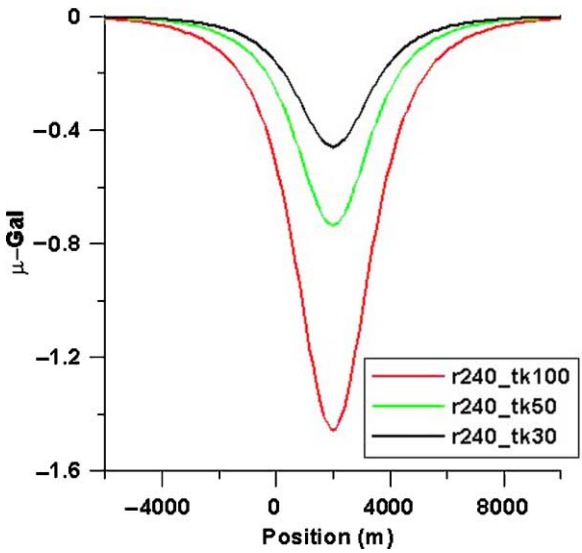

Figure 45: Surface vertical component of gravity measured over a 3D wedge at a depth of 2000 m. The wedge radius is 240 m with thickness of 100, 50, and 30 m.

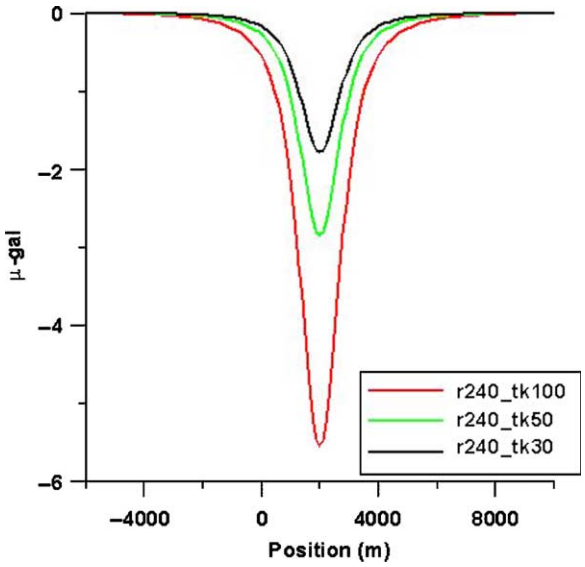

Figure 46: Surface vertical component of gravity measured over a 3D wedge at a depth of 1000 m. The wedge radius is 240 m with thickness of 100, 50, and 30 m.

the order of 1 km. The volumes affected for deeper targets will have to be much larger. These results are model-specific to the Texas gulf coast.

Tilt calculations

Recent advances in satellite imaging provide new opportunities for using land surface deformation and spectral images to indirectly map migration of CO_2. Ground surface deformation can be measured by satellite and airborne interferometric synthetic aperture radar (InSAR) systems [27,28]. Tilt meters placed on the ground surface can measure changes in tilt of a few nano-radians [29]. Taken separately or together these measurements can be inverted to provide a low-resolution image of subsurface pressure changes. While these technologies are new and have not yet been applied for monitoring CO_2 storage projects, they have been used in a variety of other applications, including reservoir monitoring [30] and groundwater investigations [30,31].

Numerical modeling work done in preparation for the DOE GeoSeq CO_2 field test in the Liberty Field, Texas provides an illustration of the application of surface deformation as a monitoring tool. The presence of the sealing faults acts to confine pressure build-up to the fault block, thus increasing the magnitude of the surface deformation.

As CO_2 injection proceeds, there is an associated pressure build up in the storage unit. This pressure increase translates into strain changes that propagate to the surface and manifest themselves as surface deformation. Figure 47 shows the change in pressure (left panel) within a 15 m thick sand unit at a depth of 1500 m from the flow simulation model of the Liberty field project as well as the inversion (right panel) of the resulting surface tilt data [30,32]. The surface tilt is shown in Figure 48. The response is dominated by the fact that the injection occurs in a bounded fault block, thus amplifying the surface tilt above the injection point. The inverted pressure distribution has captured the large-scale pressure increase trending from southwest to northeast across the center of the section. The calculated tilt values are easily observable in the field, since it is possible to achieve an accuracy of 1 nano-radian in field tilt measurements. While the limited spatial extent of this model with the presence of bounding faults (increasing the pressure buildup)

dominate the response, it is clear that these measurements can be made in the field over very small quantities of injected CO_2.

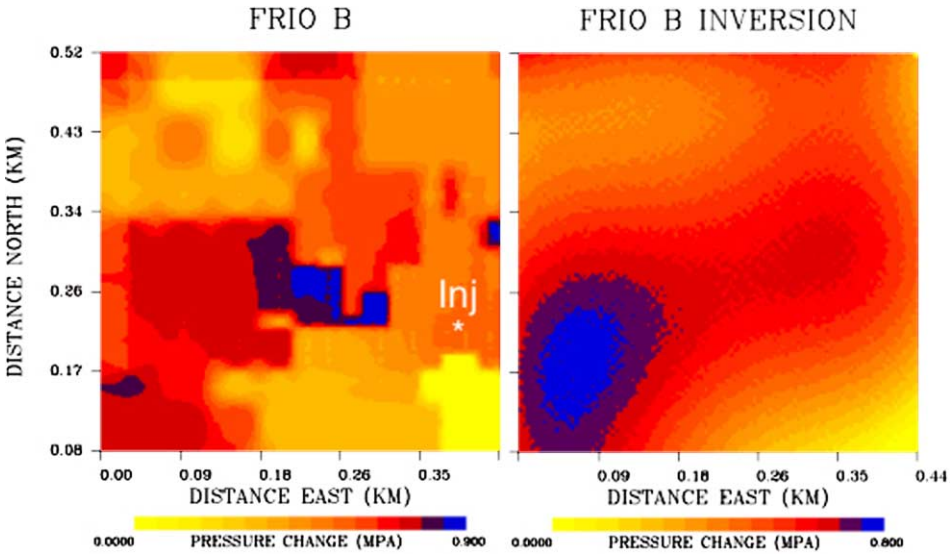

Figure 47: Left panel: pressure buildup in Frio B sand after 30 days of CO_2 injection. Right panel: inversion for pressure change from surface tilt measurements. The section shown is bounded by faults on left, right and top and is open to the bottom. CO_2 concentration is centered on the injector well but permeability variations within the unit cause the maximum pressure increase to be offset from the injection well.

The tilt measurements sensitivity to pressure changes provides an ability to map vertically integrated permeability within the injection unit. In this model the injection well is in the lower right corner of the figures. The permeability model was generated as a geostatistical realization. The model has a zone of increased permeability in the lower portions of the model below the main injection sand unit. When this unit is pressured up, the pressure front moves ahead of the injected CO_2 and pressurizes the zones with higher permeability. This causes the vertically integrated pressure change to have a maximum toward the center of the model away from the injection well. The tilt responses to this pressure increase, therefore, maps the high net permeability regions of the injection interval, ahead of the arrival of the CO_2 itself, providing a means of mapping future migration pathways.

CONCLUSIONS

Both surface and borehole gravity measurements have been modeled for Schrader Bluff. The injection of CO_2 produces a bulk density decrease in the reservoir that in turn produces a reduction in the gravitation attraction from the reservoir. The spatial pattern of the change in the vertical component of gravity (G_z) as well as the vertical gradient of gravity (dG_z/dz) is directly correlated with the net change in density of the reservoir. The difference in the vertical component of gravity on the surface caused by CO_2 injection over a 20-year period is on the order of 2 μGal, which is below the level of repeatability of current field surveys [33]. However, measurements made in boreholes just above the reservoir interval (1200 m depth) are sensitive enough to observe measurable changes in G_z as CO_2 injection proceeds. Such measurements made in numerous wells could map the areas of net density changes caused by injected CO_2 and water within

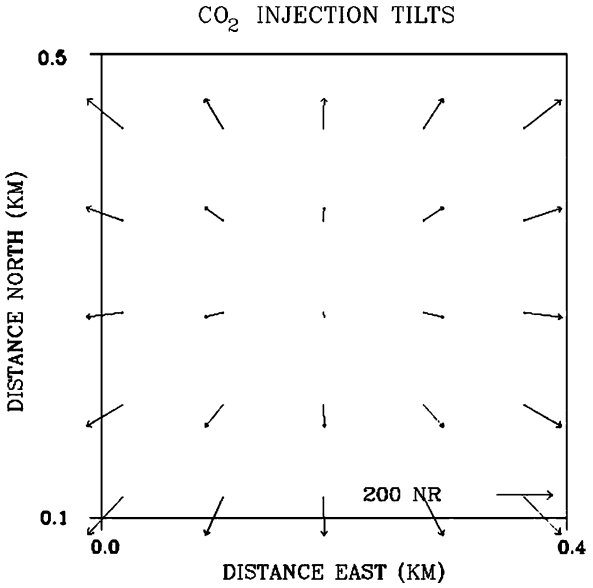

Figure 48: Surface tilt calculated for the pressure change shown in Figure 47 and rock properties representative of the Liberty Field geology. Vectors show the orientation and magnitude of the tilt. The center of the bulge over the maximum pressure is flat and has little tilt. The bounding faults truncate the pressure field and produce locations of maximum tilt.

the reservoir. The time-lapse changes in the borehole G_z and dG_z/dz clearly identify the vertical section of the reservoir where fluid saturations are changing.

There is a clear change in seismic amplitude associated with the reservoir caused by the changes in water and CO_2 saturation. In addition, there is a change in the seismic AVO effects. Both seismic amplitude and AVO can be exploited to make quantitative estimates of saturation changes, subject to modeling assumptions. Forward calculations using the isotropic Zoeppritz equation for both 2005 and 2020 models support this argument. The applications of seismic data for monitoring are covered further in Chapter 22.

The electrical resistivity of rocks is primarily a function of porosity and water saturation (S_w). When the porosity is known, or can reasonably be assumed to have small spatial variation, the changes in electrical resistivity are directly related to the changes in water saturation. EM techniques can be used to map such spatial variations in electrical resistivity. Of all the possible EM field systems, one combines both relative ease of deployment with high sensitivity to reservoirs of petroleum scale and depth. This technique uses a grounded electric dipole energized with an alternating current at a given frequency to produce time varying electric and magnetic fields that are measured on the earth's surface. This EM configuration was simulated for the Schrader Bluff model using 100 m electric dipoles operating at 1 Hz and measuring the resulting electric field at a separation of 2 km in-line with the transmitting dipole. The generated electric field for the Schrader Bluff model, using only a small portable generator is an order of magnitude above the background electric field (noise) at the operating frequency of 1 Hz. This means that synchronous detection of the signal combined with stacking can recover signal variations to better than 1%. There is a direct one-to-one correspondence with the change in S_w and the change in the electric field amplitude. While this signal level is low, it can be measured given the S/N ratio of the data. Although this represents a potential low-cost monitoring technique it is best suited for CO_2–brine systems where there is a one-to-one correlation

between the change in water saturation and the change in CO_2 saturation (since $S_w + S_{CO_2} = 1$). In petroleum reservoirs such as Schrader Bluff, the presence of hydrocarbons as additional fluids eliminates the one-to-one correlation between changes in S_w and changes in S_{CO_2}.

Electric potentials are generated when fluid flows through a porous media. Measurement of these SPs is easily done at low cost. The technique is used routinely to locate leaks in fluid containment structures such as waste pits and dams. Laboratory studies coupled with numerical simulations show that the SP coupling coefficients for CO_2 flow are large enough to cause a measurable SP signal in the field. As the CO_2 displaces water in a formation, the coupling coefficient decreases. On average, the coupling coefficients observed for CO_2 flow is about 10 times lower than for fresh water flow in the same sample. Two-dimensional steady-state calculations based on the Frio brine pilot case, using laboratory-derived coupling coefficients, indicate that the technique is a potential low-cost, low-resolution monitoring technique.

Surface and borehole tilt measurements can be used to monitor the stain changes in the reservoir and overburden associated with CO_2 injection. Inversion of the data can produce estimates of the pressure changes within the reservoir as well as estimates of permeability. While this technique has not been tested in the field over CO_2 injection sites, it offers the potential for predicting permeability pathways within the reservoir ahead of injected fluids.

The non-seismic techniques presented here show enough promises as low-cost supplements to seismic monitoring that we believe further work needs to be done to assess their spatial resolution under a wider range of conditions. A number of areas should be considered further. Borehole gravity measurements should be used in conjunction with pressure test data and/or surface seismic data to do statistical interpolation of predicted changes in S_{CO_2}. This may provide a low-cost way of monitoring changes within the reservoir with only the initial 3D seismic survey being relatively expensive. A field demonstration of the EM technique should be considered to demonstrate its potential. Surface tilt measurements coupled with pressure and injection data should be jointly tested following the work of Vasco et al. [30]. SP modeling codes that can model 3D transient multi-phase flow should be developed to more realistically address the potential of SP as a monitoring tool. SP modeling developments should be done in conjunction with field SP measurements over an injection test site. A future study of resolution that can be achieved by inversion of gravity, electrical, and SP data should be done and compared to seismic resolution.

ACKNOWLEDGEMENTS

This work was supported in part by a Cooperative Research and Development Agreement (CRADA) between BP Corporation North America, as part of the CO_2 Capture Project (CCP) of the Joint Industry Program (JIP), and the US Department of Energy (DOE) through the National Energy Technologies Laboratory (NETL), and by the Ernest Orlando Lawrence Berkeley National Laboratory, managed by the University of California for the US Department of Energy under contract DE-AC03-76SF00098.

REFERENCES

1. G. Hill, B. Moore, M. Weggeland, The CO_2 Capture Joint Industry Project: GHGT-5, Australia, 2000, pp. 248–253.
2. B.S. Brandt, A study of the speed of sound in porous granular materials, *J. Appl. Mech.* **22** (1955) 479–486.
3. G.M. Hoversten, R. Gritto, J. Washbourne, T.M. Daley, Pressure and fluid saturation prediction in a multicomponent reservoir using combined seismic and electromagnetic imaging, *Geophysics* **68** (2003) 1580–1591.
4. J. Dvorkin, A. Nur, Elasticity of high-porosity sandstones: theory of two North Sea data sets, *Geophysics* **61** (1996) 1363–1370.
5. S.L. Nooner, M.A. Zumberge, O. Eiken, T. Stenvold, G.S. Sasagawa, Seafloor micro-gravity survey of the Sleipner CO_2 sequestration site, *EOS Trans. AGU* **84** (46) (2003) Fall Meet. Suppl. Abstract GC31A-01.

6. L.A. Thomsen, J.L. Brady, E. Biegert, K.M. Strack, A Novel Approach to 4D Full Field Density Monitoring, SEG Workshop, 2003.
7. J.V. Popta, J.M.T. Heywood, S.J. Adams, D.R. Bostock, Use of Borehole Gravimetry for Reservoir Characterization and Fluid Saturation Monitoring, SPE 20896, 1990, pp. 151–160.
8. S.R. Rutherford, R.H. Williams, Amplitude-versus-offset variations in gas sands, *Geophysics* **54** (1989) 680–688.
9. J.P. Castagna, H.W. Swan, J.F. Forster, Framework for AVO gradient and intercept interpretation, *Geophysics* **63** (1998) 948–956.
10. M. Landro, Discrimination between pressure and fluid saturation changes from time-lapse seismic data, *Geophysics* **66** (2001) 836–844.
11. Shuey, A simplification of the Zoeppritz equations, *Geophysics* **50** (1985) 609–614.
12. G.E. Archie, The electrical resistivity log as an aid in determining some reservoir characteristics, *Trans. AIME* **146** (1942) 54–62.
13. S. Ellingsrud, T. Eidesmo, S. Johansen, M.C. Sinha, L.M. MacGregor, S. Constable, Remote sensing of hydrocarbon layers by seabed logging (SBL): results from a cruise offshore Angola, *The Leading Edge* **21** (2002) 972–982.
14. S.D. Hovorka, P.R. Knox, Frio brine sequestration pilot in the Texas Gulf Coast, *Sixth International Conference on Greenhouse Gas Control Technologies (GHGT-6)*, Kyoto, Japan, 1–4 October, 2002.
15. R.G. Loucks, M.M. Dodge, W.E. Galloway, Regional controls on diagenesis and reservoir quality in lower Tertiary sandstones along the lower Texas Gulf Coast, in: D.A. McDonald, R.C. Surdam (Eds.), *Clastic Diagenesis: American Association of Petroleum Geologists Memoir*, vol. 37, 1984, pp. 15–46.
16. C.W. Kreitler, M.S. Akhter, A.C.A. Donnelly, W.T. Wood, Hydrology of formations for deep-well injection, The University of Texas at Austin, Bureau of Economic Geology, Texas Gulf Coast, 1988, unpublished contract report, 204pp.
17. G.L. Macpherson, Regional variation in formation water chemistry; major and minor elements, Frio Formation fluids, Texas, *American Association of Petroleum Geologists Bulletin* **76** (5) (1992) 740–757.
18. C. Doughty, K. Pruess, Modeling supercritical CO_2 injection in heterogeneous porous media, *Proceedings*, TOUGH Symposium, May 12–14, 2003.
19. R.F. Corwin, D.B. Hoower, The self-potential method in geothermal exploration, *Geophysics* **44** (1979) 226–245.
20. D.V. Fitterman, Electrokinetic and magnetic anomalies associated with dilatant regions in a layered earth, *J. Geophys. Res.* **83** (B12) (1978) 5923–5928.
21. R.F. Corwin, H.F. Morrison, Self-potential variations preceding earthquakes in central California, *Geophys. Rev. Lett.* **4** (1977) 171–174.
22. A.A. Ogilvy, M.A. Ayed, V.A. Bogoslovsky, Geophysical studies of water leakages from reservoir, *Geophys. Prospect.* **17** (1969) 36–62.
23. V.A. Bogoslovsky, A.A. Ogilvy, Deformations of natural electric fields near drainage structures, *Geophys. Prospect.* **21** (1973) 716–723.
24. D.V. Fitterman, Self-potential surveys near several Denver Water Department dams: US Geol. Surv. Open File Report, 1983, pp. 82–470.
25. D.J. Marshall, T.R. Madden, Induced polarization, A study of its causes, *Geophysics* **24** (1959) 790–816.
26. W.B. Sill, Self-potential modeling form primary flows, *Geophysics* **48** (1983) 76–86.
27. H. Zebker, Studying the Earth with Interferometric Radar, *Comput. Sci. Engng* **2** (2000) 52–60.
28. Y. Fialko, M. Simons, Deformation and seismicity in the Coso Geothermal Area, Inyo County, California: observations and modeling using satellite radar interferometry, *J. Geophys. Res.* **21** (2000) 781-21, 793.
29. C. Wright, E. Davis, W. Minner, J. Ward, L. Weijers, E. Schell, S. Hunter, Surface tiltmeter fracture mapping reaches new depths-10,000 feet and beyond?, *Soc. Petrol. Engng* (1998) 39919.
30. D.W. Vasco, K. Karasaki, K. Kiyoshi, Coupled Inversion of Pressure and Surface Deformation Data, *Water Resour. Res.* (2001) 3071–3089.
31. J. Hoffmann, H.A. Zebker, D.L. Galloway, F. Amelung, Seasonal subsidence and rebound in Las Vegas Valley, Nevada observed by synthetic aperture radar interferometry, *Water Resour. Res.* **37** (2001) 1551.

32. D.W. Vasco, K. Karasaki, L.R. Myer, Monitoring of fluid injection and soil consolidation using surface tilt measurements, *J. Geotechn. Geoenviron. Engng* **124** (1998) 29–37.
33. J.L. Hare, J.F. Ferguson, C.L.V. Aiken, The 4-D microgravity method for waterflood surveillance: a model study from the Prudhoe Bay reservoir, Alaska, *Geophysics* **64** (1999) 78–87.
34. E. Gasperikova, G.M. Hoversten, M.P. Ryan, J.P. Kauahikaua, G.A. Newman, N. Cuevas, Magnetotelluric investigations of Kilauea volcano, Hawaii. Part I: experiment design and data processing, *J. Geophys. Res.* (2004) in review.